2015

Studies of phase change in complex systems using the generalized replica exchange method

BOSTON UNIVERSITY

COLLEGE OF ENGINEERING

Dissertation

STUDIES OF PHASE CHANGE IN COMPLEX SYSTEMS

USING THE GENERALIZED REPLICA EXCHANGE

METHOD

by

QING LU

B.S., Nankai University, 2009

Submitted in partial fulfillment of the

requirements for the degree of

Doctor of Philosophy

2015

Approved by

First Reader
_____
John E. Straub, Ph.D.
Professor of Chemistry
Professor of Materials Science and Engineering

Second Reader
_____
David Coker, Ph.D.
Professor of Chemistry
Professor of Materials Science and Engineering

Third Reader
_____
Ksenia Bravaya, Ph.D.
Assistant Professor of Chemistry

Fourth Reader
_____
Soumendra Basu, Ph.D.
Professor of Materials Science and Engineering
Professor of Mechanical Engineering

Acknowledgements

Enter through the narrow gate. For wide is the gate and broad is the road that leads to destruction, and many enter through it. But small is the gate and narrow the road that leads to life, and only a few find it.

Matthew 7:13-14

First I want to express my gratitude to my advisor, Prof. John Straub, for acepting me to his group and for guiding me throughout my doctoral study. I am thankful for his patience and encouragement. I thank my Committe, Prof. David Coker, Ksenia Bravaya, Soumendra Basu and Linda Doerrer for their time and effort to read and improve my thesis.

There have been many people in the Straub Lab who have helped me get to where I am today. I want to thank Dr. Jaegil Kim for laying down the foundation of gREM upon which I carried out my thesis work. I thank Dr. Edyta Małolepza, Laura Domínguez, Anna Victoria Martinez, Leigh Foster for many things I learnt from them. I thank everyone in the Straub group for their presence in my Ph.D study. journey.

I am grateful to my parents, and to my parents-in-law for their support in many ways. I thank my husband Xiaofei for all these years we walk together since college. I am very thankful to my family of God to whom I owe much love and prayers. Finally, I thank God for being my rock and my fortress, and the constant source of peace and hope.

STUDIES OF PHASE CHANGE IN COMPLEX SYSTEMS USING THE GENERALIZED REPLICA EXCHANGE METHOD

QING LU

Boston University, College of Engineering, 2015

Major Professor: John E. Straub, PhD
Professor of Chemistry
Professor of Materials Science and Engineering

ABSTRACT

The replica exchange method (REM) has been widely used in the computer simulation of complex systems, such as proteins, glasses, and atomic clusters, where conventional methods based on sampling the canonical ensemble struggle to attain ergodicity over a rugged energy landscape characterized by multiple minima separated by high energy barriers. While the standard temperature REM (tREM) has proven to be highly effective in the equilibrium sampling of stable single phase states, tREM is seriously challenged in the vicinity of a first-order phase transition.

The generalized Replica Exchange Method (gREM) was developed to address these outstanding computational problems and provide a method for simulating strong phase transitions in condensed matter systems. The central idea behind gREM is to incorporate the merit of generalized ensemble sampling into the replica exchange paradigm. The key ingredients of gREM are parameterized effective sampling weights, which smoothly join ordered and disordered phases with a succession of unimodal energy distributions that transform unstable or metastable energy states of the canonical ensemble into stable states that can be fully characterized. The inverse mapping between the sampling weights and the effective

temperature provides a sure way to design the effective sampling weights and achieve ergodic sampling.

Various applications of gREM are presented, including studies of the solid-liquid phase change of an adapted Dzugutov model of glass formation, the mechanism of spinodal decomposition in the vapor-liquid transition of a simple fluid, and the apparent crossover from a first-order to continuous transition with increasing density in the freezing of a nanofilm of water confined between featureless and atomistic surfaces. Extensive gREM simulations combined with the Statistical Temperature Weighted Histogram Analysis Method (ST-WHAM) demonstrate the effectiveness of the approach and provide comprehensive characterization of thermodynamic and structural properties intrinsic to phase transitions in these diverse systems.

Contents

List of Tables

List of Figures

Chapter 1

Introduction

1.1   Temperature Replica-Exchange Method (tREM)

Molecular Dynamics (MD) and Monte Carlo (MC) simulations are the two major approaches to explore the equilibrium properties of systems including liquids, bimolecules, and materials. However, straightforward MD or MC struggles to achieve ergodic sampling in systems with rugged potential energy landscapes characterized by multiple minima separated by high barriers [2, 3, 4]. It has been an objective of extensive studies to develop enhanced sampling algorithms that improve the sampling capacity of MC and MD simulations.

MC and MD simulations in an extended ensemble alogrithm represent one poweful approach for achieving efficient conformational sampling in diverse molecular systems. Three well-known extended-ensemble algorithms are the multicanonical algorithm (MUCA) [5, 6], temperature Replica Exchange Method (tREM) [7], and simulated tempering (ST) [8]. Among them, tREM is often used because the weight factor is known *a prior* (i.e., the Boltzmann factor), while those for MUCA and ST must be determined before the simulation.

In tREM [9, 10, 11, 7, 12, 13, 3], a set of statistically independent canonical molecular dynamics (MD) or Monte Carlo (MC) simulations are run in parallel at specified temperatures. Exchanges of configurations between neighboring replicas are performed subject to detailed balance. Broken ergodicity at low temperatures is significantly alleviated via configurational exchanges with high temperature replicas, which facilitate sampling the relevant configurational space without trapping.

tREM has been widely used in the computer simulation of diverse complex systems such as atomic clusters [14, 15], glasses [16, 17, 18], proteins [10, 11, 19, 20, 13, 21] and lipid bilayers [22].

1.2 Challenges for simulating strong phase transitions

While tREM has proven to be highly effective in equilibrium sampling of stable phase states, it is less applicable to systems involving strong phase transitions, in which a large energy gap may separate two macroscopic phases [23, 12, 24, 25, 26]. Canonical energy distributions in tREM are effectively disjoint and characterized by an energy gap corresponding to a latent heat. Since the acceptence probability of replica exchanges is determined by the energy overlap of neighboring replicas, an energy gap between $P_{T<T_c}(E)$ and $P_{T>T_c}(E)$ around the critical temperature T_c, $P_T(E)$ being the canonical probability density function (PDF) at temperature T, significantly impairs replica exchanges. The acceptance of replica exchanges for a pair of inverse temperatures, β and β', close to $\beta_c = 1/T_c$, becomes exponentially suppressed as $A(\beta E; \beta' E') = \min[1, e^{\Delta\beta(E'-E)}] \approx e^{-|\Delta\beta\Delta E|}$, where $\Delta\beta = \beta' - \beta$ and ΔE is the energy gap.

The failure in exploring strong phase transitions is intimately connected to a "convex intruder" in the microcanonical entropy, $S(E)$. The anomalous behavior in $S(E)$ translates into a negative slope region, the so-called "backbending" or "S-loop" [24] in the statistical temperature, T_S. The existence of the backbending has been verified in recent experiments on nuclear fragmentation [27] and cluster melting [28], and its physical origin has been attributed to avoiding a "static" phase coexistence due to the free energy cost of forming interfaces.

The energy function $E(T)$ is triple-valued in T in the "backbending" region, which means that for a given temperature in that region, three states are available to the system, including two stable states in the pure phase and one unstable state in the coexistence phase, as manifested in the bimodal structure of the probability density function, $P_T(E)$. The states in the vicinity of strong first order phase transition are intrinsically unstable for the canonical ensemble [29, 30, 31, 32, 33]. Depending on the starting structure, the system may sample one of the two stable states, but rarely samples the unstable state.

1.3 Generalized Replica Exchange Method (gREM)

The generalized Replica Exchange Method (gREM) [34] has been developed to realize the full power of replica exchange. gREM incorporates the merit of sampling from a generalized ensemble into the replica exchange paradigm. It utilizes a noncanonical ensemble to avoid the instability in the negative slope region in $T_S(E)$. A general framework was developed to systematically parameterize the sampling weights in gREM from the equilibrium phase simulation in the tREM [34]. The simplicity in the parameterization is one advantage of gREM over methods like WL-MUCA (Wang-Lauda Multicanonical), in which the sampling weight is not known *a priori* and requires a long iterative process.

Employing an inverse mapping strategy, the generalized ensemble weights are determined from effective temperatures optimally parameterized to form unique and stable crossing points with the statistical temperature. This yields a succession of unimodal energy distribution functions across the phase transition region and smoothly join the ordered and disordered phases. While the metastable and unstable states are inaccessible to tREM simulation, they are transformed into stable states through in the generalized ensemble in gREM simulation. Enhanced sampling across the metastable and unstable states is then achieved without the need to identify a "good" order parameter as for biased sampling.

Illustrative simulations on a Potts spin model [34] compared the performance of gREM and tREM around a typical first-order phase transition. tREM simulations showed two effectively disjoint sampling domains, strongly impairing the replica exchange across the phase transition region. Simulations using gREM with varying system size and simulation conditions demonstrate a comprehensive sampling for phase-coexistence states. gREM provides an order of magnitude accerlation of tunneling transitions (the round trip between the lowest and highest energy) over the WL-MUCA. It was also shown that gREM produced a correct canonical thermodynamics via reweighting at much smaller computational cost.

gREM was originally formulated in the constant volume ensemble in the benchmark work for the Potts spin system. In this work, we extend gREM to the isobaric-isothermal

ensemble to include volume fluctuation. We further apply gREM to the simulation of phase transitions in several systems, including the adapted Dzugutov model systems, Lennard-Jones fluids, and the coarsed-grained water bilayer confined in a slit nanopore. Through these applications, we investigate a diversity of phase transitions associated with these systems, and thoroughly characterized the thermodynamic and structural properties of the pure phase as well as the transition states (found in regions of metastable or unstable states in the canonical ensemble). The enhanced sampling achieved in simulations of a variety of phase transitions demonstrates the effectiveness of gREM and provides valuable insights into the phase behavior of these diverse systems.

Chapter 2

Methodology

2.1 Generalized Replica Exchange Method at constant volume

The generalized Replica Exchange Method (gREM) [34] combines generalized ensembles with replica exchanges in order to provide enhanced sampling in the vicinity of a strong phase transition.

Near the phase change region, the energy distribution, $P_\alpha(E)$, becomes bimodal due to a large energy or volume gap separating two phases, where α denotes a replica index. Sampling unstable or metastable, phase-mixed configurations becomes a rare event due to a large free energy barrier. The fundamental idea of gREM is to systematically design a set of generalized ensembles, $W_\alpha(E)$, so that unstable or metastable enthalpy states corresponding to the phase change region are transformed into stable ones, resulting in a unimodal $P_\alpha(E)$. In the most general case, the energy distribution associated with W_α is determined as

$$P_\alpha(E) = \Omega(E)W_\alpha(E) \tag{2.1}$$

where $\Omega(E)$ is the density of states in energy. By defining entropy, $S(E) = \ln \Omega(E)$ ($k_B = 1$), analogous to the entropy in the microcanonical ensemble, Eq.(2.1) further transforms into $\exp\{S(E)-w_\alpha(E)\} = \exp\{-\beta\mathcal{F}_\alpha(E)\}$, $\mathcal{F}_\alpha(E)$ being the generalized free energy density and $w_\alpha = -\ln W_\alpha$ being the generalized effective potential. The generalized partition function is obtained as $Z_\alpha(\beta) = \int dE e^{-\beta\mathcal{F}_\alpha(E)}$.

The key quantity in gREM is the effective temperature in the generalized ensemble, $T_\alpha(E;\lambda_\alpha) = [\partial w_\alpha/\partial E]^{-1}$, which completely determines the generalized sampling weight up to a constant through the inverse mapping relation

$$\ln W_\alpha(E) = -\int^E \frac{1}{T_\alpha(E';\lambda_\alpha)}dE' \tag{2.2}$$

where λ_α is a set of parameters characterizing the effective temperature. It is possible to identify conditions for the effective temperature ensuring that the underlying unstable state will be transformed into the stable energy state with a unimodal probability density function (PDF), $P_\alpha(E)$.

A necessary and sufficient condition on $T_\alpha(E; \lambda_\alpha)$ is derived by identifying an extremum, E_α^*, of a generalized free energy density, $\beta \mathcal{F}_\alpha(E) = w_\alpha(E) - S(E)$,

$$T_\alpha(E_\alpha^*; \lambda_\alpha) = T_S(E_\alpha^*) = T_\alpha^*, \tag{2.3}$$

where $T_S(E) = [\partial S / \partial E]^{-1}$ is the statistical temperature in energy analogous to the statistical temperature in the microcanonical ensemble and E_α^* is the crossing point between $T_\alpha(E)$ and $T_S(E)$. By identifying a stability condition

$$\beta \mathcal{F}_\alpha''(E_\alpha^*) = (\gamma_S - \gamma_\alpha)/T_\alpha^{*2}, \tag{2.4}$$

where $\gamma_S = T_S'(E_\alpha^*)$, $\gamma_\alpha = T_\alpha'(E_\alpha^*)$, and the prime denotes differentiation with respect to E, we find that a unimodal PDF can arise about the unique crossing point, E_α^*, between $T_S(E)$ and $T_\alpha(E; \lambda_\alpha)$, subject to the condition that $\gamma_\alpha(E_\alpha^*) < \gamma_S(E_\alpha^*)$. A schematic plot of the effective temperatures that form unique crossing points with the statistical temperature with the backbending behavior across the transition region is shown in Fig. 2.1.

In gREM, exchange between neighboring replicas is performed in which replicas represent noncanonical ensembles characterized by the effective temperature $T_\alpha(E; \lambda_\alpha)(\alpha = 1, 2, ..., M)$. As the parameter λ_α varies, $T_\alpha(E; \lambda_\alpha)$ covers a range of temperature between T_1 and T_M, T_1 and T_M being the lowest and highest temperature. Based on the one-to-one correspondence, the sampling weight $W_\alpha(E, \lambda_\alpha)$ is completely determined by the inverse mapping in Eq. (2.2).

The simplest parameterization scheme for forming stable crossing points between the effective temperature, $T_\alpha(E; \lambda_\alpha)$, and the statistical temperature, $T_S(E)$, is to align linear
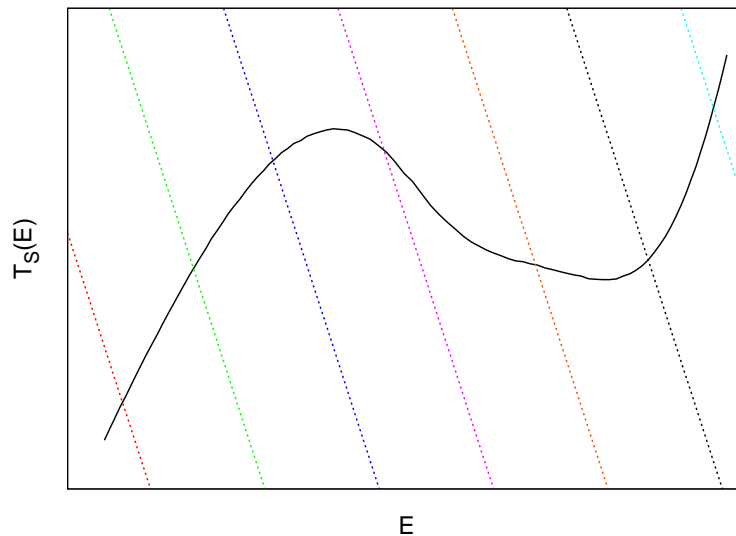
Figure 2.1: The black solid curve is a schematic plot of the statistical temperature, $T_S(E)$, with a backbending region. The set of parallel dashed lines represent the linear effective temperatures of gREM.

effective temperatures in parallel with the constant slope, γ, as

$$T_\alpha(E; \lambda_\alpha) = \lambda_\alpha + \gamma(E - E_0), \tag{2.5}$$

the control parameter λ_α being the T-intercept at an arbitrarily chosen E_0. To form the unique stable crossing point E_α^* in each replica, γ must be less than the minimum slope $\gamma_S^{\min}$, $\gamma_S^{\min} = \min\{T_S'(E)\}$ being the minimum slope of $T_S(E)$ for the sampled energy region. Since $T_S(E)$ is monotonically increasing except for the phase change region, in most cases a proper γ is easily guessed from the approximate $T_S(E)$ by connecting a few points of $[\tilde{E}(T), T]$, $\tilde{E}(T)$ being an average energy of a short canonical run at T. For example, γ can be simply chosen as $\gamma = (T_M - T_1)/(\tilde{E}_1 - \tilde{E}_M)$, T_1 and T_M being the lowest and highest temperature, and $\tilde{E}_\alpha = \tilde{E}(T_\alpha)$.

Once γ is fixed, the dynamic range of λ_α is determined to cover the interesting temperature range between T_1 and T_M as $\lambda_1 = T_1$ and $\lambda_M = T_M - \gamma(\tilde{E}_M - \tilde{E}_1)$, with $E_0 = \tilde{E}_1$. The first and Mth effective temperatures are chosen to cross $[\tilde{E}_1, T_1]$ and $[\tilde{E}_M, T_M]$, respec-

tively. The intermediate values of λ_α ($1 < \alpha < M$) are determined by equally dividing the parameter space as

$$\lambda_\alpha = \lambda_1 + (\alpha - 1)\Delta\lambda \tag{2.6}$$

and $\Delta\lambda = (\lambda_M - \lambda_1)/(M - 1)$.

The linear effective temperature of Eq. (2.5) produces the generalized sampling weights as

$$W_\alpha(E; \lambda_\alpha) \sim [\lambda_\alpha + \gamma(E - E_0)]^{-1/\gamma}. \tag{2.7}$$

Detailed simulation protocols of the gREM are defined by the following three steps.

(i) Perform short canonical runs at several temperatures between T_1 and T_M to determine the data set, $[\tilde{E}_\alpha, T_\alpha]$. Select a proper γ to be less than the minimum slope of the statistical temperature T_S, and determine λ_α by employing Eq.(2.6) between $\lambda_1 = T_1$ and $\lambda_M = T_M - \gamma(\tilde{E}_M - \tilde{E}_1)$, with $E_0 = \tilde{E}_1$.

(ii) Run the gREM simulation in each replica by making Monte Carlo trial moves in configuration space with the acceptance probability

$$A_{\text{intra}}(\mathbf{x} \to \mathbf{x}') \quad = \quad \min[1, e^{w_\alpha(E) - w_\alpha(E')}], \tag{2.8}$$

where the effective potential $w_\alpha(E) = -\ln W_\alpha$, W_α being the sampling weight.

A Monte Carlo trial move consists of an attempted single particle displacement. For constant pressure ensemble, the volume move is also performed after N trial single particle displacements are made, where N equals the number of particles.

After all replicas finished N attempted single particle displacements and a trial volume move, attempt a replica exchange between neighboring replicas with the acceptance

$$A_{\text{inter}}(\alpha; \mathbf{x}\mathbf{x}') = \min\left[1, \exp(\Delta_\alpha)\right], \tag{2.9}$$

with $\Delta_\alpha = w_{\alpha+1}(E') - w_{\alpha+1}(E) + w_\alpha(E) - w_\alpha(E')$.

(iii) Once a sufficiently long production run has been performed, calculate the entropy estimate $\tilde{S}(E)$ by joining multiple generalized ensemble runs via the weighted histogram analysis method (WHAM) [35] or statistical temperature weighted histogram analysis method (ST-WHAM) [36].

2.2 Generalized Replica Exchange Method at constant pressure

To incorporate volume fluctuations in the simulation of solid-liquid phase change, we extend the gREM to the isothermal-isobaric ensemble. In contrast to the constant volume ensemble where the internal energy, E, of the system is a natural dynamic variable at the fixed volume V, the enthalpy $H = E + PV$, which describes the thermal energy change when a process occurs at constant pressure, P, becomes the key dynamical variable in the constant pressure ensemble.

We focus on the density of states $\Omega(H; P)$ as a function of the enthapy as

$$\Omega(H; P) = \int dV \int d^3 r \delta[H - (E + PV)], \tag{2.10}$$

with the entropy $S(H; P) = k_B \ln \Omega(H; P)$. We apply the inverse mapping strategy to design optimal Tsallis weights $W_\alpha(H; \lambda_\alpha)$ from the effective temperature $T_\alpha(E) = \lambda_\alpha + \gamma(H - H_0)$ in the two-dimensional (H, T) plane. With a proper choice of γ, $T_\alpha(E)$ will form stable crossing points with $T_S(E)$ at H_α^*, $T_\alpha(H_\alpha^*) = T_S(H_\alpha^*) = T_\alpha^*$, allowing direct access to metastable and unstable states in the phase transition region.

2.3 Statistical Temperature Weighted Histogram Analysis Method (ST-WHAM)

Since each replica in gREM samples a configurational space with the non-canonical sampling weight, all simulation results should be combined to estimate correct canonical averages via a reweighting. The Statistical Temperature Weighted Histogram Analysis Method (ST-

WHAM) [36, 37, 38] is utilized to combine multiple generalized ensemble runs to determine the entropy estimate. Once the entropy is determined, all canonical thermodynamic averages are determined for any temperature by the reweighting technique. Contrary to the conventional Weighted Histogram Analysis Method (WHAM) [35], ST-WHAM does not require an iterative process to determine relevant partition functions, and directly determines the inverse statistical temperature estimate, $\beta_S(E) = 1/T_S(E)$, by utilizing the sampling weights used in the gREM simulations, $W_\alpha(E)$, and associated histograms of energy, $h_\alpha(E)$, which are the results of gREM simulations.

The entropy estimate $S(E)$ or corresponding density of states estimate is computed from a numerical integration of $\beta_S(E) = \partial S(E)/\partial E$, enabling a substantial acceleration of the data analysis without loss in accuracy. The ST-WHAM estimate for the inverse statistical temperature is obtained as

$$\beta_S = \sum_\alpha f_\alpha(E)\left(\frac{\partial \ln h_\alpha}{\partial E} - \frac{\partial \ln W_\alpha}{\partial E}\right), \tag{2.11}$$

where $h_\alpha(E)$ is the energy histogram in replica α, $f_\alpha(E) = h_\alpha(E)/\sum_\alpha h_\alpha(E)$ is the simulated histogram fraction. Due to the rapid variation of β_S for small E a direct integration of β_S is not desirable so we first approximate the statistical temperature $T_S(E)$ on equally spaced energy grids, allowing a piecewise analytical integration [36]. All canonical thermodynamic properties are completely determined from the calculated $S(E)$.

The Helmholtz free energy density at a given temperature T is calculated by $F_T(E) = E - TS(E)$ and the reweighted probability density function is given by $P_T(E) = e^{-F_T(E)/T} = e^{S(E)-E/T}$. The canonical expectation value for any quantity is computed as

$$\langle A(T)\rangle = \frac{\int dE\, e^{S(E)-\beta E}A(E)}{\int dE\, e^{S(E)-\beta E}}, \tag{2.12}$$

and the canonical heat capacity is estimated through the energy fluctuation as

$$C(T) = \frac{\langle E(T)^2 \rangle - \langle E(T) \rangle^2}{k_B T^2}.$$ (2.13)

If the constant pressure ensemble is used instead of the constant volume ensemble, the natural dynamical variable is replaced by the enthalpy instead of energy in all the equations shown above for ST-WHAM.

Chapter 3

Exploring the solid-liquid phase change of an adapted Dzugutov model using generalized Replica Exchange Method

3.1 Introduction

We apply gREM to explore the phase change properties of an adapted Dzutugov model system. This is a one-component system with a model metallic pair potential and is kown to be an ideal glass former that avoids crystallization at any cooling rate [39, 40]. The molecular dynamics simulation performed by Elenius and Dzugutov [40] reported a polyamorphous phase transition from a liquid to a phase with a mesoscopic-range order similar to that of a smectic liquid crystal and the rate of structural relaxation characteristic of the glassy state. In this chapter, we test the effectiveness of gREM for achieving enhanced sampling while exploring thermodynamic changes and structural transformations associated with the phase change in the adapted Dzugutov model system[1].

3.2 Methods

3.2.1 Simple monatomic Dzugutov model

We apply gREM to study the solid-liquid phase change properties of a single-component system with an adapted Dzugutov potential (donoted as Z2) [39, 41]. The Z2 potential has the form

$$V(r) = a\frac{e^{\alpha r}}{r^3}\cos(2k_F r) + b(\frac{\sigma}{r})^n + V_0 \tag{3.1}$$

for $r < r_c$ and 0 otherwise. We use the position of the third minimum in the function as our cutoff distance, r_c, and V_0 is defined through the equation $V(r_c) = 0$. V_0 acts to shift the

---

[1]Much of the material presented in this chapter appears in Q. Lu, J. Kim and J. E. Straub, *Journal of Physical Chemistry B*, **116**, 8654 (2012)

Table 3.1: Values of the parameters for the Z2 potential.

a	α	k_F	b	σ	n	r_c	V_0
1.04	0.33	4.139	4.2×10^6	0.348	14.5	2.64488	0.13391543

potential so that it vanishes at the third minimum, thus making the function and its first derivative continuous at the cutoff. The potential is plotted in Fig. 3.1 together with the Lennard-Jones potential, and the values of the parameters for the potential [41, 40] are given in Table 3.1. We use a system of 500 identical particles and set the pressure to be $P = 0.40$ for all replicas in order to simulate the NPT ensemble rather than NVT ensemble explored previously for this model system [39]. Using constant pressure simulation in the vicinity of a phase change, the system is free to transform completely into the state of lowest free energy, which may not be achieved in constant volume simulation. All simulation results are expressed in reduced units of length and energy which are defined by the Z2 pair potential, the main repulsive part of which closely approximates that of the Lennard-Jones potential. Considering the Lennard-Jones potential as a model potential of argon, and the mass of the argon atom as the unit of mass, the reduced units of length and energy can be estimated as 0.34 nm and 0.238 kcal/mol [40].

The Z2 potential was designed to imitate effective interionic interactions in liquid metals with characteristic Friedel oscillations [42, 43]. The first term in the potential has a form similar to that expected for the effective interaction between metal ions screened by electrons. Friedel oscillations are present with wave vector $2k_F$, where k_F corresponds to the wave vector at the Fermi level. The second term adds a repulsive interaction that suppresses the oscillations at small r. The potential has been found to induce a pronounced local icosahedral ordering of the nearest neighbors due to the design of its short-range attraction, while the repulsion incorporated in the longer-range interaction inhibits bulk packing of icosahedra.
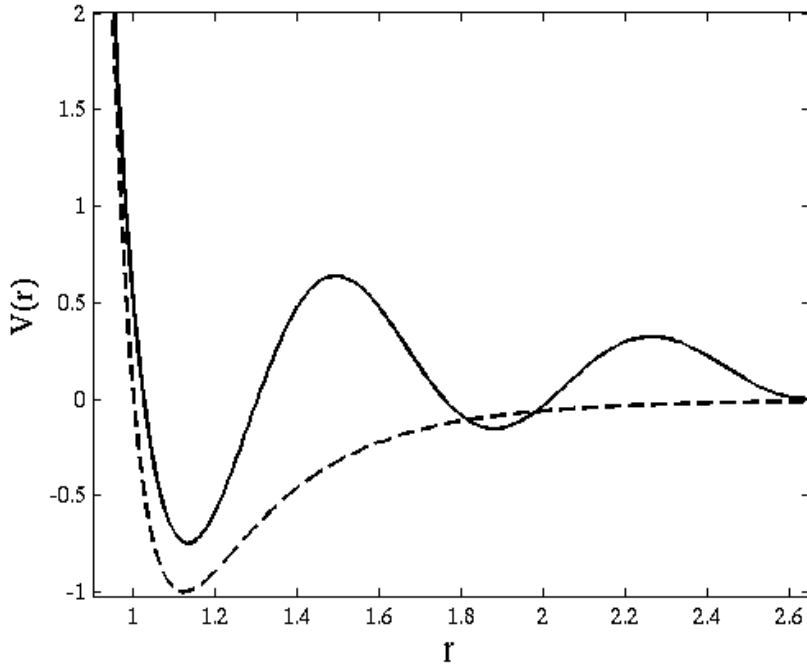
Figure 3.1: The Z2 potential (Ref. 22,23) used in this study (solid line) compared to the Lennard-Jones potential (dashed line). Plotted after Fig. 1 in Ref. 23.

3.2.2 Measuring the sampling convergence using the ergodic measure

The energy metric is a convenient quantity to assess the time intervals needed for effective ergodicity to be established by following the dynamics of a system using two distinct initial conditions [44]. The energy metric $d(t)$ is defined in terms of time averages of energies of individual particles. The time-averaged potential energy of particle j over a trajectory is computed as

$$e_j(t) = \frac{1}{t} \int_0^t E_j(s)ds \tag{3.2}$$

where $E_j(s)$ is the energy of particle j at time s on the trajectory. Because the potential energy in this study is pairwise additive, $E_j(s)$ is one-half of the sum of all potential-energy terms involving particle j. Two independent initial states of the system are chosen, and these are labeled a and b. The energy metric, $d(t)$, is given by the square of the energy

difference between the energy averages of the particles over the two trajectories, namely,

$$d(t) = \frac{1}{N} \sum_{j=1}^{N} [e_{ja}(t) - e_{jb}(t)]^2 \tag{3.3}$$

where the sum runs over all N particles of the system. For an ergodic system, we expect that $\lim_{t \to \tau} [e_{ja}(t) - e_{jb}(t)] \to 0$ for each particle j. This is because the time averages for the system reach their equilibrium values in a time τ independent of any initial condition. In practice, an acceptable estimate for τ is obtained by determining when $d(\tau)/d(0) = 0.01$ is satisfied [44].

The behavior of $d(t)$ for times greater than a transient time t_I is characterized by a single parameter, D_E, "diffusion constant" associated with the rate of exploration of phase space. The decay of $d(t)$ for $t > t_I$ has been shown to obey the dynamical scaling form

$$d(t) = d(0)f(tD_E) \tag{3.4}$$

where

$$f(x) = \begin{cases} 1 & x \to 0 \\ 1/x & x \gg 1 \end{cases}$$

The reciprocal of D_E is roughly the time required for effective ergodicity to be obtained.

To apply the ergodic measure in the replica exchange method, one must compute the measure for each replica separately, because the replicas are at different temperatures and the sampling speeds will, in general, depend on temperature or underlying generalized ensemble. Two independent initial states are given to each replica $\alpha = 1, ..., M$, and the two trajectories (a, α) and (b, α) are generated. The energy metric for replica α is computed as

$$d^{\alpha}(t) = \frac{1}{N} \sum_{j=1}^{N} [e_{ja}^{\alpha}(t) - e_{jb}^{\alpha}(t)]^2 \tag{3.5}$$

where e_{ja}^{α} is the time averaged energy of particle j, computed using Eq. (3.2), and the superscript α indicates replica α.

3.2.3 Probing structure change using pair distribution functions

The radial distribution function is computed from the simulation trajectories as

$$g(r) = \frac{1}{\rho_0 N} \left\langle \sum_{i=1} \sum_{j \neq i} \delta(r - r_{ij}) \right\rangle \tag{3.6}$$

where ρ_0 is the bulk density, r_{ij} is the distance between atom i and j , and $\langle \cdots \rangle$ denotes an ensemble average.

Let us denote the first minimum of $g(r)$ as r_1. The coordination number, which is the average number of neighbors, CN, up to a distance r_1, can be computed as [45]

$$CN = 4\pi\rho_0 \int_0^{r_1} r^2 g(r) dr \tag{3.7}$$

as the area under the first peak of $r^2 g(r)$ is proportional to the number of particles in the first coordination shell.

The static structure factor $S(Q)$ is related to a Fourier transform of the radial distribution function $g(r)$ [46, 47] according to

$$S(Q) = 1 + 4\pi\rho_0 \int_0^L r^2 \left(\frac{\sin(Qr)}{Qr} \right) [g(r) - 1] dr \tag{3.8}$$

The wave vector Q is defined as $Q = 2\pi k/L$, where k is an integer that ranges from 1 to N, N is the total number of particles, and L is the length of periodic boundary box. $S(Q)$ provides a measure of the correlation length of the density fluctuations.

3.2.4 Identifying structural symmetry through bond orientational order parameters

Bond orientational order parameters [48, 49, 50] based on spherical harmonics, also known as Steinhardt order parameters, are often used to determine crystal structures in molecular simulations. In computational studies of crystallization from an undercooled liquid, one must distinguish particles that are part of the crystal from those that belong to the liquid. Ideally, such an assignment is based on the local environment of the particles only. One method, which is independent of the specific crystal structure and does not require the definition of a reference frame, is provided by the following algorithm based on spherical harmonics.

The complex vector $q_{lm}(i)$ of particle i is defined as $q_{lm}(i) = \frac{1}{N_b(i)} \sum_{j=1}^{N_b(i)} Y_{lm}(\mathbf{r}_{ij})$, where, $N_b(i)$ is the number of nearest neighbors of particle i, the functions $Y_{lm}(\mathbf{r}_{ij})$ are the spherical harmonics, and $\mathbf{r}_{ij}$ is the vector from particle i to particle j. To make the order parameters invariant with respect to rotations of the reference frame, the third-order invariants are defined as

$$w_l(i) = \sum_{m_1+m_2+m_3=0} \begin{pmatrix} l & l & l \\ m_1 & m_2 & m_3 \end{pmatrix} q_{lm_1}(i)q_{lm_2}(i)q_{lm_3}(i) \tag{3.9}$$

where the coefficients $(\cdots)$ are the Wigner $3j$ symbols. We refer to the normalized quantity

$$\hat{w}_l \equiv \frac{w_l}{\left(\sum_m |q_{lm}|^2\right)^{3/2}}. \tag{3.10}$$

Using this approach, one can determine the type of crystalline structure occuring around each individual particle.

3.3 Results and Discussion

3.3.1 Effective temperatures and generalized ensemble distributions

To determine the dynamic range of λ_α and the optimal value of γ we first performed short canonical Monte Carlo simulations for 2×10^4 MC sweeps (MCS), at $T_1 = 0.3$ and $T_M = 0.6$, which determine $\tilde{H}_1 = -0.7157$ and $\tilde{H}_M = 2.0128$. One MC sweep includes N trial moves, N is the number of particles, and M is the total number of replicas ($M = 31$). The value of γ is computed as $\gamma = (T_M - T_1)/(\tilde{H}_1 - \tilde{H}_M) \approx -0.11$. Setting $H_0 = \tilde{H}_1$ in Eq. (2.5), the dynamic range of λ_α, between $\lambda_1 = T_1$ and $\lambda_M = T_M - \gamma(\tilde{H}_M - \tilde{H}_1)$, depends on γ. For $\gamma = -0.11$, $\lambda_1 \approx 0.30$ and $\lambda_M \approx 0.72$.

The generalized sampling weights can be determined by Eq. (2.7) once the parameters γ and λ_α are known. Replica exchanges were attempted after every replica completed one MC sweep. Resulting effective temperatures (solid lines) in 3.2(a) were chosen to fully span the phase change region. For comparison, we also plot the exact $T_S(H)$, which was determined by the statistical temperature weighted histogram analysis method (ST-WHAM) [36]. All relevant parameters in the gREM have been chosen based on short canonical runs at T_1 and T_M and full knowledge of $T_S(H)$ is not necessary.

Since $T_\alpha(H; \lambda_\alpha)$ was designed to form a unique, stable crossing point, H_α^*, with $T_S(H)$, the resulting generalized probability distribution functions (GPDFs) in 3.2(b) are rapidly localized around a given H_α^* with a Gaussian shape, and naturally bridge between ordered and disordered phases with unimodal energy distributions across the change region. Since $P_\alpha(H)$ is sharply peaked at H_α^*, $T(H_\alpha^*; \lambda_\alpha) = T_S(H_\alpha^*)$, the set of most probable energies, $[H_\alpha^*, T_\alpha^*]$, asymptotically converges toward a locus of $T_S(H)$. Indeed, the profile of $[H_\alpha^*, T_\alpha^*]$ shows a perfect coincidence with $T_S(H)$ determined by ST-WHAM, and exactly corresponds to crossing points between $T_S(H)$ and $T_\alpha(H; \lambda_\alpha)$ in 3.2(a). For convenience, the most probable energy H_α^* was approximated by the average energy summed over the αth replica. For each individual replica, the enthalpy distribution function $P_\alpha(H)$ has a single peak

around H_α^* with a Gaussian shape.
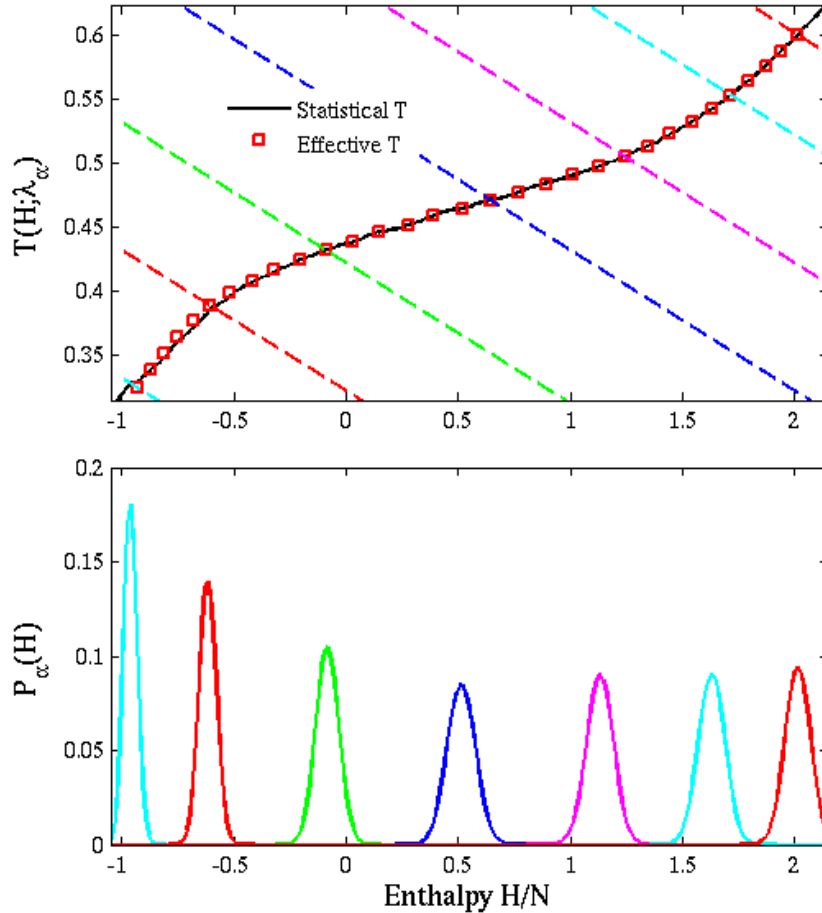
Figure 3.2: (a) Most probable energy set $[H_\alpha^*, T_\alpha^*]$ (red squares) determined by gREM for 10^7 MCS, and statistical temperature $T_S(H)$ (black solid line). Here H_α^* is the average enthalpy of replica α and T_α^* is the effective temperature. The parallel dashed lines represent $T(H; \lambda_\alpha)$ linear effective temperatures of replica α. (b) Probability distribution functions $P_\alpha(H)$. In both (a) and (b), $\alpha = 1, 6, 11, 16, 21, 27, 31$ from left to right. Same colors are applied for the same simulations in both panels.

3.3.2   Sampling speed evaluated using the ergodic measure

We have demonstrated the effectiveness of gREM to achieve comprehensive sampling. In this section we examine the sampling efficiency of gREM compared with traditional tREM using

ergodic measure to quantify the sampling speed and rate of convergence of thermodynamic averages.

The energy metric and reciprocal metric are computed using Eqs. (3.2) and (3.3) by following two sets of energy trajectories with two independent initial conditions. As stated earlier, the energy metric for an ergodic system is expected to behave as $\frac{d(t)}{d(0)} = \frac{1}{D_E t}$ so that reciprocal metric scales as $\frac{d(0)}{d(t)} = D_E t$. The diffusion constant, D_E, measures the sampling speed in phase space. Our results in Fig. 3.3 confirm that the reciprocal metric is a linear function of time for both tREM and gREM, and the slope of the reciprocal metric of gREM, which gives the diffusion constant D_E, is nearly two times greater than that of tREM.
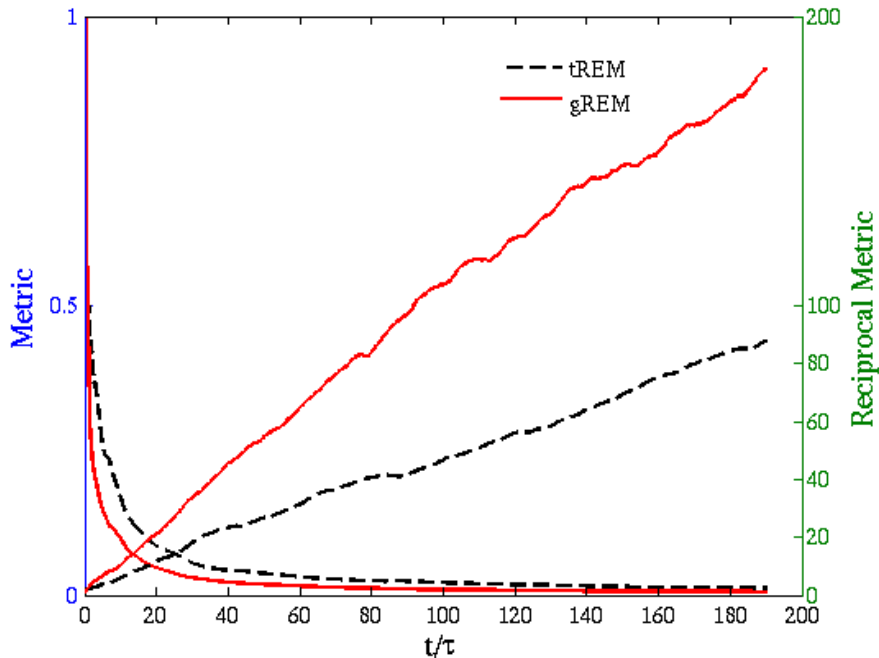
Figure 3.3: Energy metric $d(t)/d(0)$ and reciprocal metric $d(0)/d(t)$ of tREM (black dash line) and gREM (red solid line) are shown for the $17th$ replica. The simulation time t is scaled by τ, the equilibrium time step, which equals to 3×10^4 MC sweeps.

We computed the diffusion constants $D_E(\alpha)$ of all replicas ($\alpha = 1, ..., M$) for tREM and gREM. In tREM, temperature of αth replica is $T_\alpha = T_1 + (\alpha - 1)\Delta T$, where $\Delta T = (T_M - T_1)/(M - 1)$, T_1 and T_M being the lowest and highest temperature. In gREM,

the most probable effective temperature T_α^* was computed by Eq. (2.5) as $T_\alpha(H; \lambda_\alpha) = \lambda_\alpha + \gamma(H_\alpha^* - H_0)$, where the most probable enthalpy H_α^* was approximated by the average enthalpy summed over the αth replica. As the D_E and temperature of each replica are known, we can plot D_E against the temperature at that replica. Fig. 3.4 presents the D_E of tREM and gREM as a function of temperature within T=[0.3,0.55]. Similar results were observed for gREM and tREM. At low temperatures $T = [0.3, 0.45]$, D_E stays at a low value when temperature increases. Once temperature goes beyond $T = 0.47$, D_E begins to increase dramatically. There is a three order of magnitude difference between the diffusion constant D_E of the lowest and highest temperature. This indicates that the system undergoes a phase change from liquid to amorphous solid upon cooling from $T = 0.6$ to 0.3. Note that the reciprocal of D_E in Fig. 3.4 also provides an estimated time scale for each replica to reach effective ergodicity.
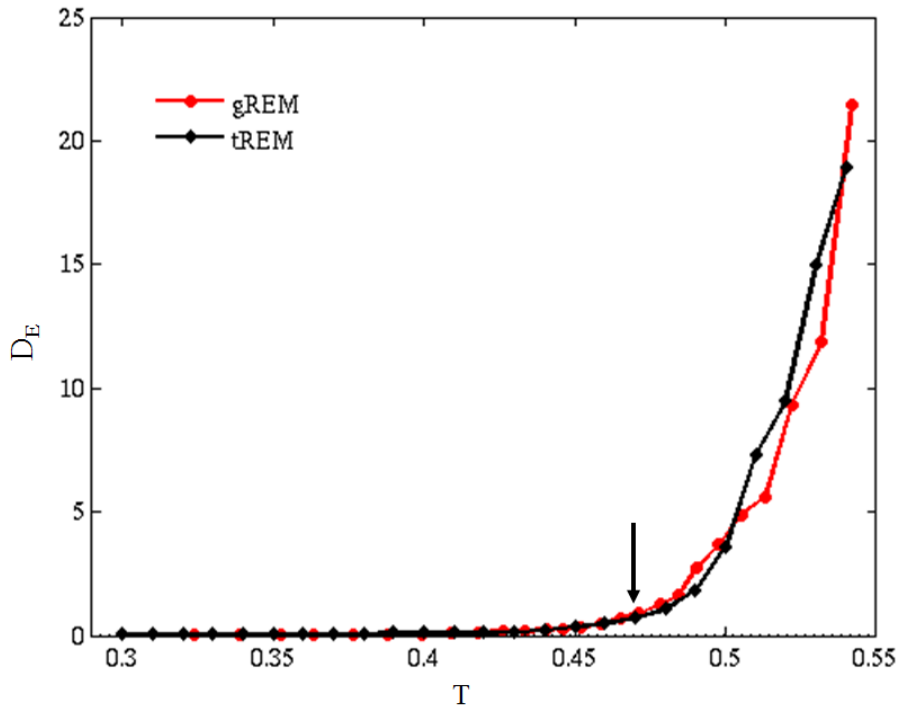
Figure 3.4: The temperature variation of diffusion constant D_E for both gREM (red) and tREM (black). The vertical arrow indicates the melting temperature.

3.3.3   Investigation of liquid-solid phase change

The thermodynamic phase change and phase change temperature were investigated, structurally by calculating the radial distribution function, and thermodynamically by computing the temperature variation of the specific heat.

The radial distribution function $g(r)$ is an appropriate tool to describe the short-range order in a monatomic liquid, providing the probability density of finding two atoms in the liquid at a separation r. The computed $g(r)$ of the liquid displays a prominent first peak centered at the nearest-neighbor spacing in the crystalline solid indicating the existence of substantial short-range order $g(r)$. The short-range ordering decreases at high temperature due to thermal fluctuation and increases at low temperature. As shown in Fig. 3.5 (a) from the bottom to the top curve, the first peak of g(r) grows taller as temperature decreases. The second and third peaks also become more visible as temperature drops. Meanwhile, the location of each peak remains the same regardless of the temperature. It is worthwhile to point out that even at the lowest temperature T=0.3, $g(r)$ shows characteristics of the liquid state. In the crystalline state, $g(r)$ has an infinite number of sharp peaks whose separations and heights are characteristic of the lattice structure. In the liquid state, the second peak is less prominent and the third peak is hardly visible in $g(r)$, indicating a lack of long-range order. Correlations in particle positions rapidly die out in a liquid and $g(r)$ approaches unity over a distance of a few particle diameters.

The static structure factor $S(Q)$ can be computed through the Fourier transform of the radial distribution function $g(r)$ by Eq. (3.8). Fig. 3.5 (b) presents the results of $S(Q)$ showing that at all temperatures S(Q) has a nearest neighbor peak located around $Q \approx 2\pi$. Below the location of the nearest neighbor peak, there is an additional low-Q prepeak, indicating the formation of the clustering and the resulting residual repulsive interaction between clusters. The presence of the low-Q prepeak in $S(Q)$ at a finite wavevector, highlights the presence of an additional characteristic length scale in this system[51]. Under cooling, the height of the prepeak increases and the width becomes narrower. However, the similarity
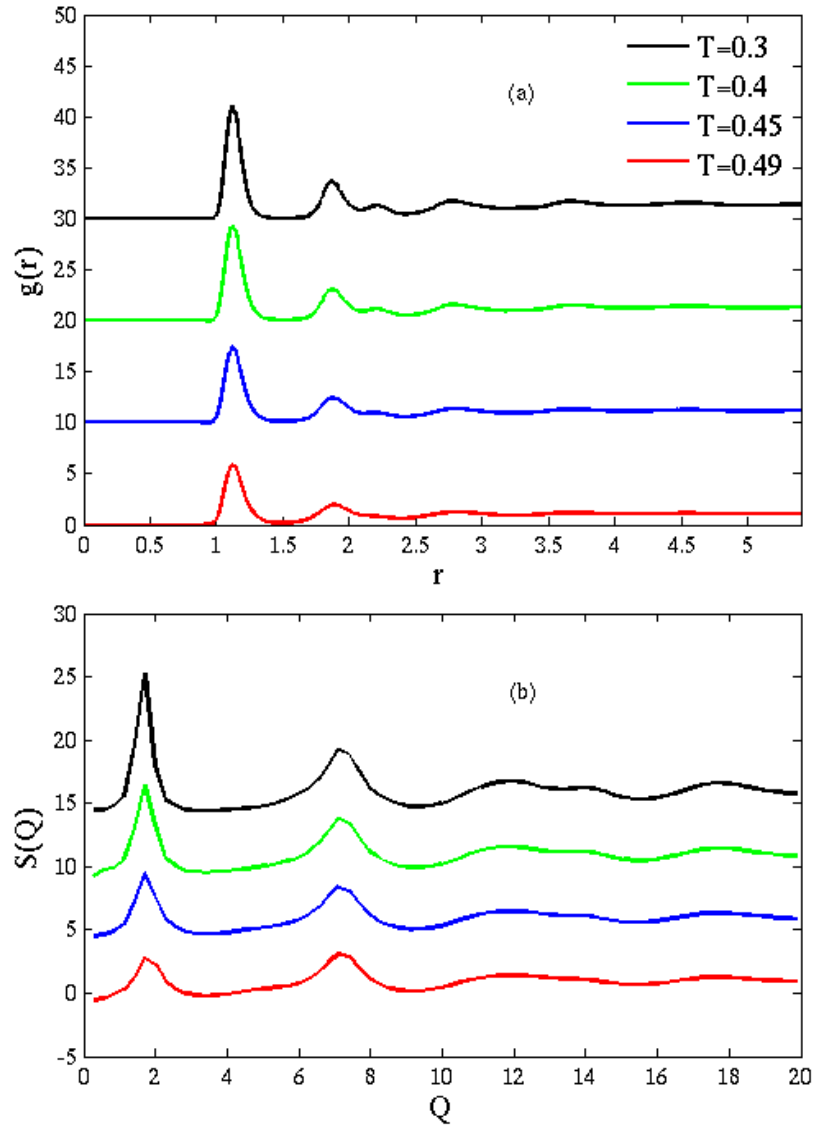
Figure 3.5: (a)Radial distribution function $g(r)$ and (b) structure factor $S(Q)$at four different temperatures as noted in (a), where r is distance and Q is wavevector. The same color scheme is used for the same temperature in both (a) and (b).

of the curves indicates that we observe a phase change between two similarly structured phases.

The coordination number (CN) measures the average number of nearest neighbors, and reflects the degree of short-range order in a system. Fig. 3.6 shows the temperature variation

of the coordination number, which shows a gradual decrease as the temperature increases. At low temperature $T = 0.3, CN \approx 10$ indicating that on average each particle has 10 nearest neighbors. The short-range ordering is characteristic of the solid state, but as discussed earlier, the steady decay of $g(r)$ to unity at large distances indicates the lack of long-range ordering. The nature of the low temperature state is determined to be an amorphous solid state. As temperature increases, CN drops dramatically, reflecting the system is melting near a characteristic temperature around $T = 0.47$.
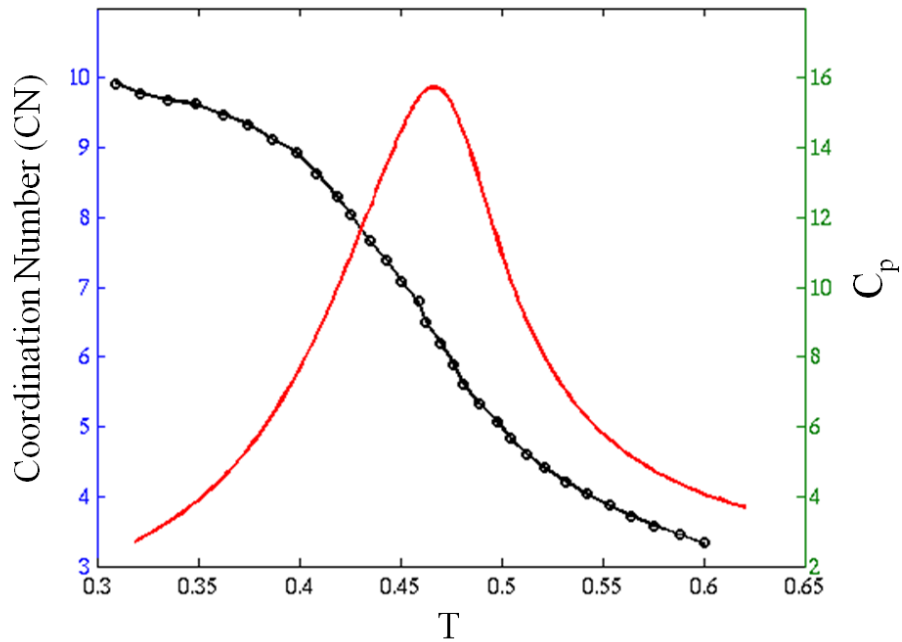
Figure 3.6: Temperature variation of coordination number (CN) and specific heat (C_p) near the phase change temperature in black and red lines respectively.

The temperature variation of the specific heat at constant pressure, C_p, is also shown in Fig. 3.6, displays a pronounced maximum at $T = 0.47$. The appearance of excess specific heat under cooling is an indication of the development of bonded structure, and a common precursor of bond percolation [42, 43]. The maximum of C_p, as well as the low-Q prepeak of $S(Q)$, is commonly observed in the context of gelation in colloidal systems [52, 51].

The maximum temperature $T_m = 0.47$ is in agreement with the phase change temperature derived from the coordination number.

3.3.4 Assessing icosahedral cluster formation using bond order parameters
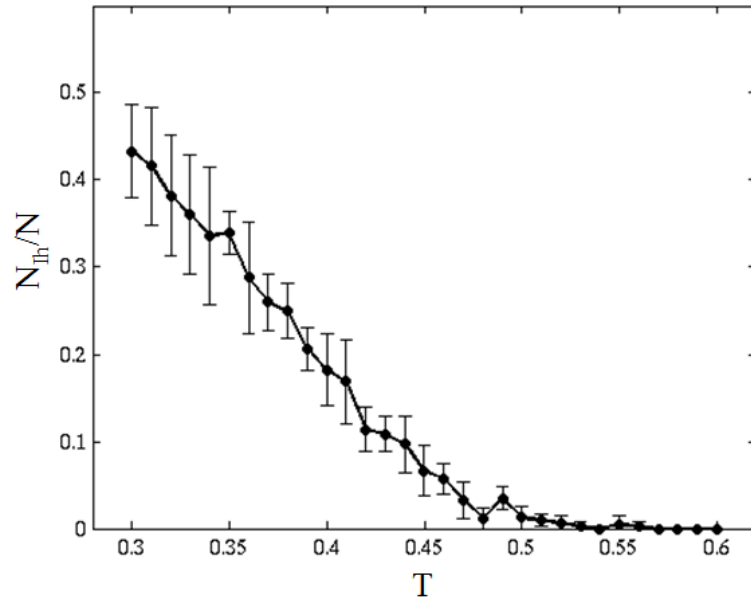
Figure 3.7: The number of particles showing local icosahedral structure N_{Ih} scaled by the total number of particles (N) in the system as a function of temperature between T=[0.3,0.6]. The error bars are defined as the standard deviation from 9 sets of independent results.

Bond-orientational order parameters were computed to determine the nature of the local symmetry underlying the local order observed at low temperatures. The four bond order parameters $q_4, q_6, \hat{w}_4$ and $\hat{w}_6$ are generally sufficient to identify crystal structures reflecting fcc,bcc,hcp and Ih (icosahedra) structure. We focus on icosahedral local ordering which is a pronounced feature of this adpated Dzugutov model system. Local icosahedral ordering is characterized by large negative values of $\hat{w}_6$, up to $\hat{w}_6 = -0.1675$ for a perfect icosahedron [48].

The value of $\hat{w}_6$ for each individual particle is computed using Eq. (3.9). If $\hat{w}_6 \leq -0.165$,
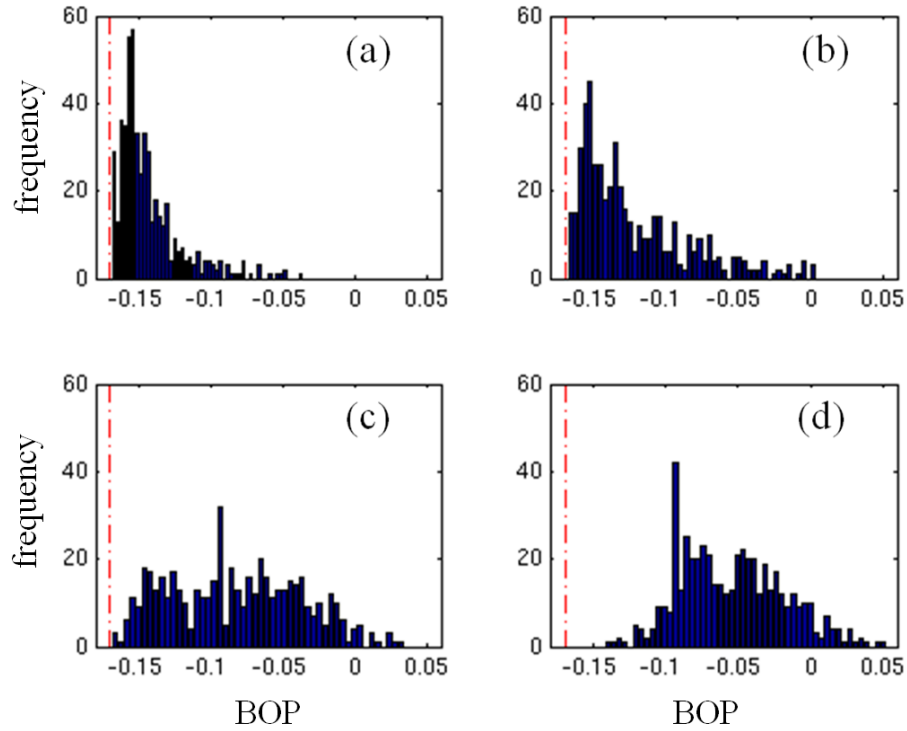
Figure 3.8: The distribution of bond order parameter $\hat{w}_6$ at four temperatures T=0.3, 0.4, 0.5, 0.6, (a, b, c, d) respectively. The red dashed line is the reference value of $\hat{w}_6$ for the ideal icosahedral symmetry.

the particle is counted as icosahedrally ordered, and its nearest neighbors within a cutoff radius of 1.5 are also included in the icosahedral cluster. In Fig. 3.7 we present the computed temperature variation in the number of icosahedrally coordinated particles, N_{Ih}, scaled by system size N. The value of N_{Ih}/N remains almost temperature independent for $T > 0.5$, and grows rapidly with cooling below $T = 0.47$, which is also the location of the maximum in the the specfic heat, C_p. This phase change temperature is coincident with the bond percolation threshold, where the bonds are defined between pairs of atoms that are nearest neighbors in icosahedral clusters. At low temperature $T = 0.3$, nearly 50% of the particles belong to icosahedral clusters.

Fig. 3.8 shows the distributions of $\hat{w}_6$ at four temperatures across the phase change range. The reference value for ideal icosahedral ordering is plotted as a red dashed line. At

$T_1 = 0.3$, $\hat{w}_6$ has a sharp and narrow peak located close to the reference value, indicating that a large percentage of particles have icosahedral local ordering. At $T_2 = 0.4$, the peak of the $\hat{w}_6$ distribution remains close to the reference value, but the distribution becomes wider. Increasing the temperature further to $T_3 = 0.5$ and $T_4 = 0.6$, the icosahedral symmetry is mostly absent.
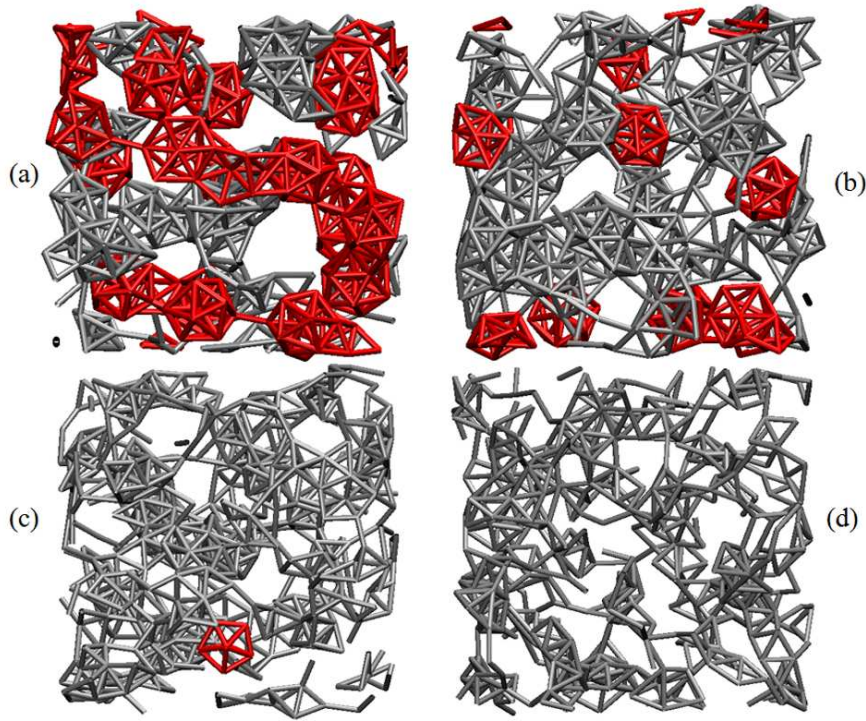
Figure 3.9: Four respresentative configurations at four temperatures T=0.3, 0.4, 0.5, 0.6, (a, b, c, d) respectively. The icosehedral clusters are marked in red and the nonicosahedral particles are marked in gray. The cutoff distance for a bond is 1.5. Note that the size of each plot does not represent the real volume at that temperature.

Insight into the structral transformation from solid to liquid is provided by direct inspection of the atomic configurations. Fig. 3.9 depicts four configurations at $T_1 = 0.3$ to $T_4 = 0.6$. At T_1 the connected icosahedral clusters occupy a large percentage of the volume. At $T_2 = 0.4$, the number of icosahedral clusters is diminished and the icosahedra are scattered and disjoint. When $T_3 = 0.5$, the number of icosahedral clusters is further diminished. As temperature increases to $T_4 = 0.6$, the icoshedral ordering is found to be absent

in the high temperature liquid state. These results are consistent with earlier observations regarding the evolution of icosahedral order in this system under cooling (see Fig. 3.7).

3.4   Conclusion

The applicability of the generalized Replica Exchange Method (gREM) has been demonstrated in an adapted Dzugutov model system. By combining optimally parameterized generalized ensemble sampling with the replica exchange protocol, the gREM provides effective sampling across the phase change region through succesive unimodal energy distributions. The ergodic measure comparison between gREM and tREM reveals the advantage of gREM in achieving effective conformational sampling across the phase change region. The diffusion constant computed by the ergodic measure shows a three order of magnitude difference between the highest and lowest temperature state, indicating that the system undergoes a liquid to amorphous solid phase transition upon cooling. The temperature evolution of the radial distribution function and structure factor demonstrates that the low temperature state is not a crystalline solid, but rather an amorphous solid possessing short-range icosahedral order. The phase change temperature was determined to be $T = 0.47$ through evaluation of the temperature variation of the coordination number and specific heat through the solid-liquid phase change. The growth of icosahedral clustering under cooling is observed and quantified with the aid of bond order parameters.

Our results indicate that the solid states of lowest free energy for the range of pressures studied have an amorphous character and lack long-range translational symmetry characteristic of an ordered solid. The adapted Dzugatov potential imposes characteristic length-scales that will be reflected in a structured liquid or solid, including the core particle size (dictated by the repulsive potential), the position of the first minimum, and the distance between the first and second potential minimum (or intervening maxima) resulting from the potential oscillations. The solid state is characterized by the formation of iscoahedral clusters, the size of which is largely determined by the core particle size and position of the first

potential minima. These "super-particles" are then found to arrange themselves on a lattice geometry, where the distance between lattice sites will be determined by the interactions between superparticles. Depending on the relation between the positions of second and third minima and maxima and the overall icosahedral superparticle size, the interactions may be stabilized or result in frustration. With the parameterization of the adapted Dzugatov model studied in this work, which was tailored to prevent crystallization [41], these competing lengthscales lead to frustration that disrupts long-range order. Optimization of these interactions and parameters could potentially lead to a thermodynamically stable solid state exhibiting long-range translational order, as well as a stronger and more cooperative transition between the liquid and solid states.

The absence of a substantial difference in the measured rate of conformational sampling for gREM as opposed to tREM results from the modest nature of the solid-liquid phase change in this system and the absence of a substantial energy gap. As a result, the distribution of states in energy or enthalpy is relatively continuous for temperature replicas as well as for the generalized energy distributions. The gradual nature of this phase change is in part due to the amorphous nature of the observed solid state which lacks long range translational order. More dramatic enhancements in sampling using the gREM protocol can be expected for systems demonstrating stronger phase transitions with a more substantial energy gap and a range of unstable states in the canonical ensemble.

Chapter 4

Order parameter free enhanced sampling of the vapor-liquid transition using the generalized Replica Exchange Method

4.1 Introduction

Application to the study of an adapted Dzutugov model explored the effectiveness of gREM in sampling a solid-liquid phase transition [53]. In this work, gREM is used to study the vapor-liquid phase transition in Lennard-Jones fluids, which has been the subject of extensive studies [54, 55, 56, 57, 58, 59].

Originally, gREM was formulated at constant volume where the internal energy of the system is a natural dynamical variable. However, in most vapor-liquid transition experiments the pressure, or, equivalently, the chemical potential of the vapor, is held constant [60, 61, 62]. Approaches informed by classical nucleation theory (CNT) usually consider the formation and growth of a liquid droplet at constant pressure [63, 64, 65]. In this work, gREM is extended to the constant pressure constraint as an essential step for the effective simulation of the vapor-liquid transition.

In a standard NPT ensemble the liquid cluster cannot coexist stably in the vapor phase. The liquid cluster that is bigger than the critical size will grow in order to minimize the excess free energy, while the cluster that is smaller than the critical size will shrink, in order to lower the excess free energy. Ten Wolde and Frenkel [60, 66] used a biased Monte Carlo ("umbrella sampling") approach to stabilize large droplets. Schrader, Virnau and Binder [67] used the successive umbrella sampling to observe the liquid droplets coexisting in stable thermal equilibrium with supersaturated vapor at a range of densities. While these methods are successful in probing metastable states associated with the liquid-vapor transition, they rely on the identification of a "good" order parameter for the transition,

to exploit in the application of biased sampling, which can be difficult to identify in more complex systems [68].

The gREM approach allows effective sampling of metastable and unstable states in the vapor-liquid coexistence states, independent of knowledge of an effective order parameter for the transition. In a gREM simulation, each stage of the phase transition can be stabilized, including the formation of a liquid droplet, the growth of a liquid cluster, and vanishing of the vapor phase. Recently, a crossover from a purely nucleation-controlled processes to a spinodal decomposition was predicted for LJ fluids in a deeply supercooled regime [69, 70]. Since we are able to observe the whole transition process through gREM simulation, we can effectively assess the mechanism of the vapor-liquid phase transition at various conditions[1].

4.2   Lennard-Jones fluid

We study the vapor-liquid phase transition in a Lennard-Jones system [71] in which the interaction potential was truncated and shifted at a cutoff radius $r_c = 2.5\sigma$, where σ is the particle diameter. The energy of interaction φ between any two particles separated by a distance r is given by

$$\varphi(r) = \begin{cases} \varphi_{\mathrm{LJ}}(r) - \varphi_{\mathrm{LJ}}(r_c) & r < r_c \\ 0 & r \geq r_c \end{cases}$$

where $\varphi_{\mathrm{LJ}}(r) = 4\epsilon(\sigma^{12}/r^{12} - \sigma^6/r^6)$ is the full LJ interaction, ϵ and σ are the LJ well depth and diameter, and $r_c = 2.5\sigma$ is the interaction cutoff separation. We made no long-range corrections and applied cubic periodic boundary conditions. The Lennard-Jones parameters were used to reduce all the variables including the temperature, $T^* = Tk/\epsilon$, enthalpy, $H^* = H/\epsilon$ and density, $\rho^* = \rho\sigma^3$. The numerical values for argon are $\sigma = 0.3405$ nm, $\epsilon = 119.8$ K.

---

[1]Much of the material presented in this chapter appears in Q. Lu, J. Kim and J. E. Straub, *Journal of Chemical Physics*, **1382**, 104119 (2013)

gREM simulations were carried out for systems at seven pressures and with two different sizes, 250 and 1000 particles. For the simulations of $N = 1000$ and $N = 250$ systems, 99 replicas are used, and the other parameters are in Table 4.1 and 4.2.

Table 4.1: Parameters in the gREM simulation for N=250 system

Pressure	H_0	λ_1	λ_M	$\gamma_0(\times 10^{-3})$
0.0078	-1224.0	0.7	6.4	-3.8765
0.016	-1223.1	0.7	4.5	-2.5998
0.03	-1217.1	0.7	2.8	-1.3225
0.04	-1218.6	0.7	5.1	-2.9046
0.06	-1214.9	0.7	1.7	-3.6717
0.08	-1209.7	0.7	1.7	-3.8646
0.096	-1208.7	0.7	1.7	-4.0646

Table 4.2: Parameters in the gREM simulation for N=1000 system

Pressure	H_0	λ_1	λ_M	$\gamma_0(\times 10^{-4})$
0.0078	-4891.0	0.7	6.4	-9.6976
0.016	-4884.9	0.7	2.9	-3.6221
0.03	-4877.2	0.7	2.8	-3.3001
0.04	-4874.3	0.7	1.9	-1.4536
0.06	-4853.6	0.7	1.7	-9.1983
0.08	-4842.5	0.7	1.7	-9.6842
0.096	-4829.7	0.7	1.7	-1.0187

4.3 Results and Discussion

4.3.1 Sampling effectiveness

A comparative study was performed between gREM and tREM simulations in order to explore the difference in sampling effectiveness. The simulations were performed at pressure $P = 0.04$ for a system with 250 particles, and number of replicas $M = 99$ in both tREM and gREM simulations. For tREM, the temperature of each replica was equally allocated

between the lowest and highest temperature $T_1 = 0.7$ and $T_M = 1.1$. The effective temperature of gREM obeys $T_\alpha(H) = \lambda_\alpha + \gamma(H - H_0)$. The parameters in the effective temperature are $H_0 = -1218.6$, $\lambda_1 = 0.7$, $\lambda_M = 5.1$ and $\gamma_0 = -0.0029046$.

In the strong first order phase transition, the statistical temperature $T_S(H)$ exhibits a negative slope, the so-called backbending or S-loop. Instead of using canonical temperatures, gREM uses effective temperatures in order to form unique stable crossing points with the statistical temperature, T_S. The linear effective temperatures of different replicas, T_α, are aligned in parallel with a constant slope γ, which is less than the slope of T_S in the backbending region. As a result, unique crossing points are formed between T_α and T_S throughout the enthalpy range of interest.
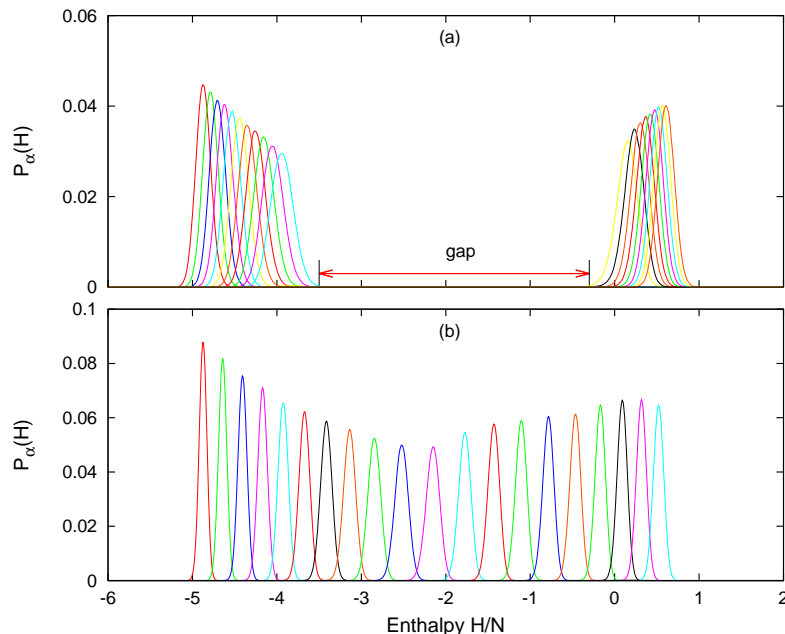
Figure 4.1: (a) and (b) show the resulting generalized probablity distribution functions (GPDF) of replica $1, 11, \cdots 91$ and 99 sampled by tREM and gREM, respectively. The enthalpy gap in tREM is marked in (a).

Since $T_\alpha(H; \lambda_\alpha)$ was designed to form a unique, stable crossing point, H_α^*, with $T_S(H)$, the resulting PDFs are sharply localized around H_α^* with a Gaussian shape in Fig. 4.1(b), and naturally bridge the vapor and liquid phases with unimodal enthalpy distributions

across the transition region. In contrast, the canonical enthalpy distributions of tREM are effectively disjoint by an enthalpy gap corresponding to the latent heat between vapor and liquid phases, which is displayed in PDFs in Fig. 4.1(a). As a side note, the actual overlaps between enthalpy distributions of neighboring replicas are greater than what is observed in Fig. 4.1, since only 10 out of 99 replicas are plotted in Fig. 4.1.

During the simulations, we kept track of the movement of replicas of both tREM and gREM in the enthalpy space. Fig. 4.2 shows the trajectories of replica 61 and 14 of both tREM and gREM. While the tREM trajectories sample two narrow ranges in enthalpy space, the trajectories of gREM reach the lowest and highest boundaries and span the enthalpy space. The tunneling transitions [72] in the two replicas and other replicas (not shown) enable the mixing between the high and low enthalpy configurations. The gREM simulation achieves comprehensive sampling in the phase transition region, while tREM fails because of the intrinsic instability of canonical ensemble in the backbending region.
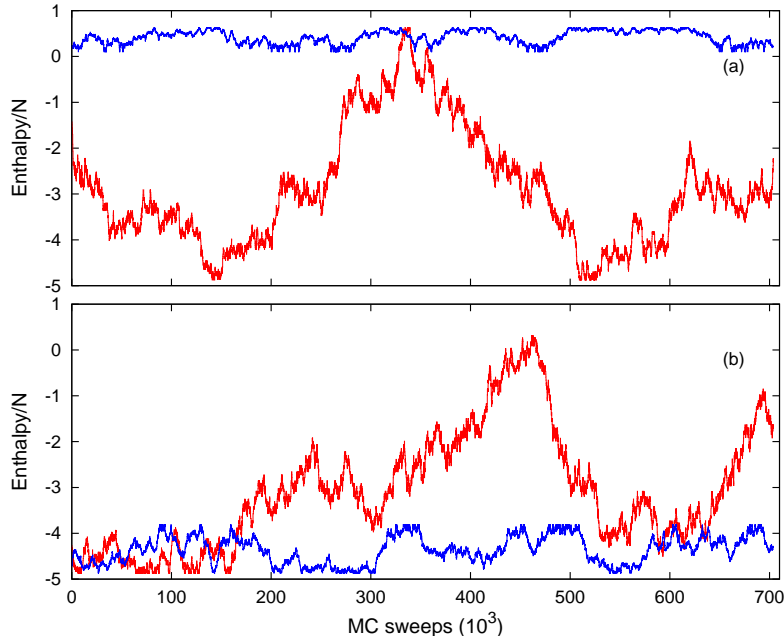
Figure 4.2: (a)The enthalpy trajectories of replica 14 in tREM (blue line) and gREM (red line). (b) The enthalpy trajectories of replica 61 in tREM (blue line) and gREM (red line).

4.3.2 Vapor-liquid phase coexistence properties and phase diagram

gREM simulations were carried out for systems at seven pressures and with two different sizes, 250 and 1000 particles, exploring temperatures as functions of enthalpy and density, $T(H)$ and $T(\rho)$, and liquid-vapor coexistence points and spinodal points at each pressure.

The line of equilibrium coexistence of two phases in a one-component system corresponds to equalities of the pressures, temperatures and the chemical potentials of the liquid and vapor phases. At equilibrium, the Gibbs free energy difference, $\Delta G = (H_{\text{vap}} - H_{\text{liq}}) - T \int_{\text{liq}}^{\text{vap}} dS = 0$, H_{vap} and H_{liq} being the enthalpy of vapor and liquid phases at the coexistence temperature. Given that the statistical temperature $T_S(H) = (\partial H/\partial S)_{N,P}$, integration yields $\Delta S = \int_{H_{\text{liq}}}^{H_{\text{vap}}} dH/T_S(H)$. Therefore, the coexistence temperature must satisfy:

$$\frac{\Delta G}{T} = \frac{H_{vap} - H_{liq}}{T} - \int_{H_{liq}}^{H_{vap}} \frac{dH}{T_S(H)} = 0. \tag{4.1}$$

Eq.(4.1) is equivalent to the Maxwell equal area rule. The equilibrium temperatures on the coexistence curve are determined through this method.

For the simulations of $N = 1000$ and $N = 250$ systems, 99 replicas are used, and the other parameters are in Table 4.1 and 4.2. The critical temperature, T_c, and density, ρ_c, can be obtained through fitting the coexistence points to Guggenheim-type equations [73, 1]. For $N = 250$ system, $T_c = 1.0780$ and $\rho_c = 0.3198$ and for $N = 1000$ system, $Tc = 1.0730$ and $\rho_c = 0.3224$. Vrabec et al. reported similar values as $T_c = 1.0779$ and $\rho_c = 0.3190$. The coexistence and critical points of these three systems are shown in Fig. 4.4.

While crossing the phase coexistence of binodal curve, the system enters the metastable phase, which retains its restorative reaction to small perturbations of density [55]. The conditions of stability against this kind of perturbation is violated only when the system reaches the spinodal, which is the locus of points surrounding the unstable region [74]. The spinodal points can be simply identified by the maximum and minimum of the $T(H)$ and $T(\rho)$ curves as shown in Fig. 4.3 (a) and (b). On $T(\rho)$ curves, the regions enclosed by
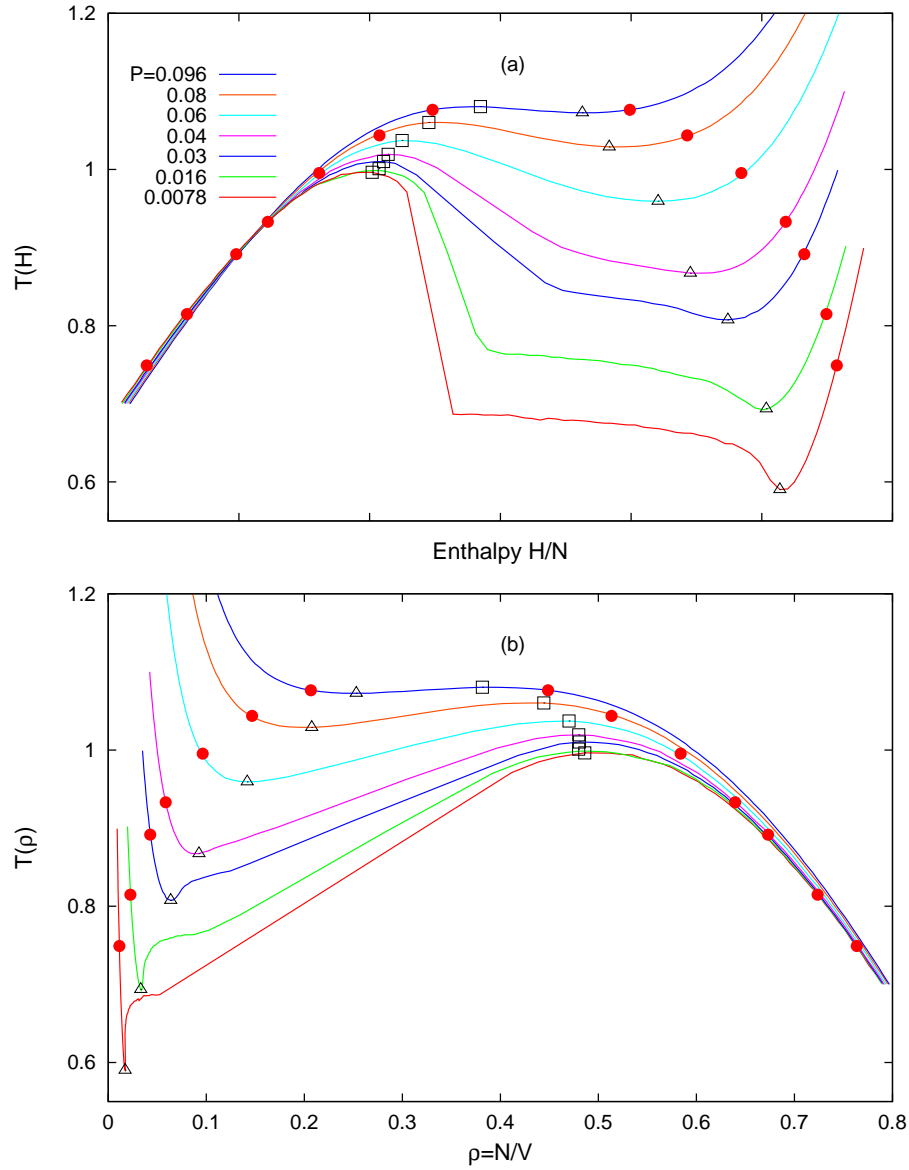
Figure 4.3: (a)Temperatures $T(H)$ as functions of enthalpy at seven different pressures for systems with 250 particles. The liquid-vapor coexistence temperature and enthalpy points (T_{CE}, H_{CE}) are plotted as red filled circles. The black open squares and triangles denote liquid and vapor spinodal points, respectively. (b) Temperatures $T(\rho)$ as functions of density at seven different pressures. Same colors and symbols are used for the same simulations in both (a) and (b).

spinodal points have positive slopes which give the negative thermal expansion coefficients as the characteristics of unstable phases.

The degree of backbending in the $T(H)$ curve gradually decreases as the pressure increases. At some low pressures, like $P1 = 0.0078$, the transition region of $T(H)$ displays severe backbending. When the pressure reaches $P7 = 0.096$, which is close to the critical pressure [75], the backbending is almost transformed into an inflection and the first order phase transition becomes second-order, in agreement with the theoretical prediction for the behavior at the critical point.
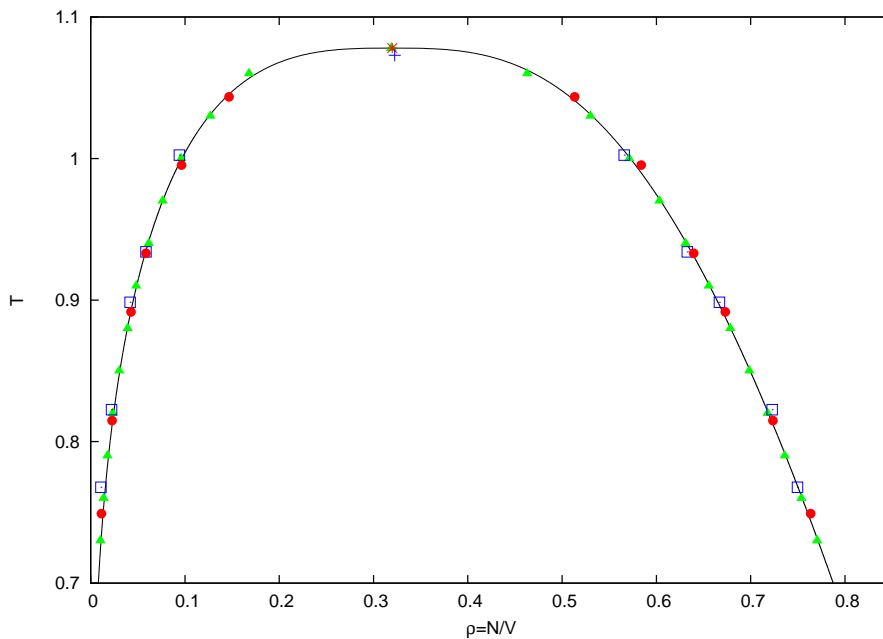
Figure 4.4: The coexistence temperatures and densities of the $N = 250$ system are plotted with red filled circles, and that of the N=1000 system is plotted as blue squares. The critical temperature and density for $N = 250$ and $N = 1000$ system is denoted by the red star and blue cross, respectively. The error bars for the present simulations are smaller than the figure symbols. The critical and coexistence points reported by Vrabec *et al.* [1] are in green filled triangles.

4.3.3 Thermodynamic properties calculated from ST-WHAM

We employed ST-WHAM to compute the entropy and subsequently the Gibbs free energy for the system of 1000 particles. The temperature variation of Gibbs free energy per particle, $G(T)/N$, at pressure $P = 0.03$ is shown in Fig. 4.5. The Gibbs function intersects itself at

point D, which is the liquid-vapor coexisting point and the liquid and vapor phases are the sections on the left and right side of point D, respectively. The liquid and vapor curves are connected together through the intermediate states on the kink where the curvature changes sign. Following Callen [76], we refer to the kink on the Gibbs function as the closed loop. The discontinuity of the curvatures of liquid and vapor curves is the characteristic of a first order phase transition.
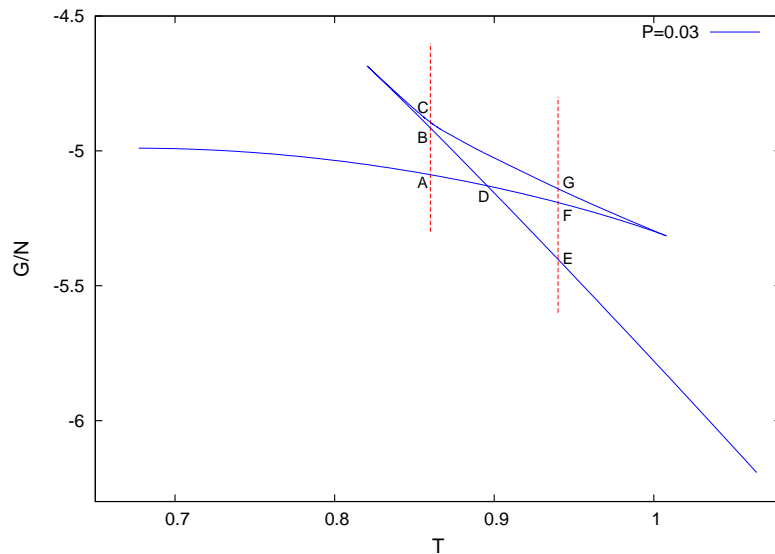
Figure 4.5: The temperature variation of Gibbs free energy per particle, $G(T)/N$, at pressure $P = 0.03$. The letters $A - G$ denotes the states on the Gibbs function.

The closed loop results from the fact that enthalpy function, $H(T)$, is triple-valued in T for the backbending regime. For a given temperature, three states are available to the system, as, for example, the states designated by A, B and C. Among these three states, state C is unstable to small fluctuations in density. A and B are stable, and the Gibbs function is a local minimum. In generalized ensemble sampling, such as gREM simulation, the metastable and unstable states like state B and C are transformed into stable states. Similarly, the Gibbs function is tripled-valued at another temperature, where states E, F and G, are stable, metastable and unstable states, respectively, in the canonical ensemble.

We have shown that backbending in $T(H)$ curves decreases with the increasing pressure
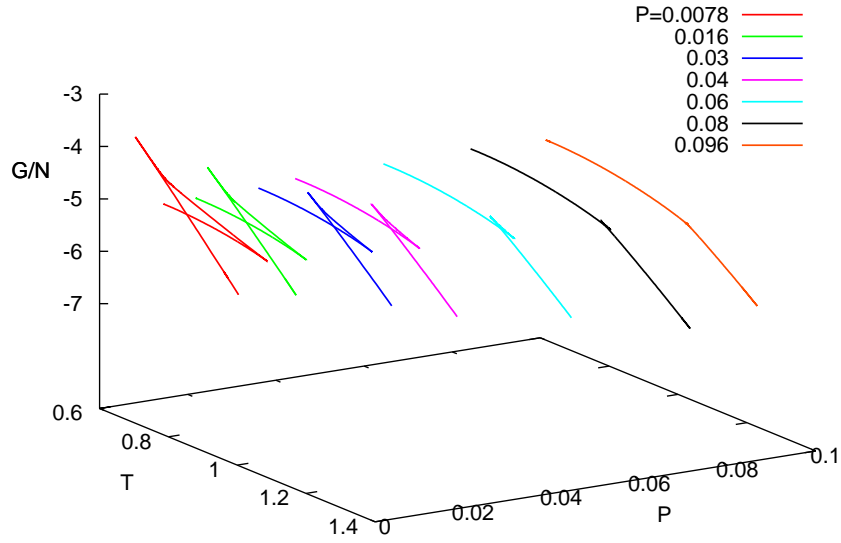
Figure 4.6: Behavior of the Gibbs free energy per particle, $G(T)/N$, as a function of temperature at seven different pressures.

in Fig. 4.3. Because the closed loop in $G(T)/N$ curves are the result of the backbending in $T(H)$, we expect the closed loop will shrink when the pressure increases. Fig. 4.6 presents the evolution of the Gibbs function at seven different pressures. The closed loop is large at the low pressures, becomes smaller with increasing pressure, and at $P = 0.096$ the closed loop almost disappears. With the diminishment of the closed loop, the Gibbs functions of the liquid and vapor phases are connected continuously, and the liquid-vapor phase transition becomes a second order continuous phase transition.

4.3.4 Structural properties

It is known that nucleation and continuous phase transition are the two mechanisms that control the first-order and second-order phase transitions, respectively. Direct inspection of the atomic configurations will validate the statement. The configurations of the system at a lower pressure, $P3 = 0.03$, and near the critical pressure, $P7 = 0.096$, are shown in Fig. 4.7 and Fig. 4.8, respectively. The vapor particles are marked in red and the liquid particles

are in gray. Stillinger's criterion [77] was used to determine whether a particle is liquid-like or vapor-like, and the cutoff radius is $r_c = 1.5$. The results presented in this section are for systems with 1000 particles.
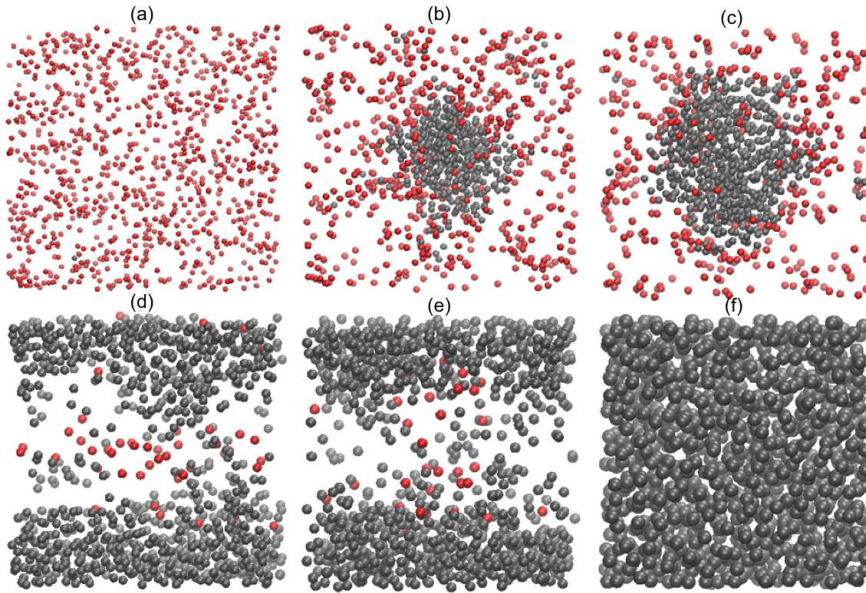
Figure 4.7: Configurations of 6 different states throughout the phase transition at $P3 = 0.03$. The vapor particles are in red and the liquid particles are in gray. Note that the size of each box is not proportional to the volume of the state.

Representative configurations spanning the vapor-liquid transition, including the pure vapor state, "droplet" states, "bubble" states and the pure liquid state, are shown in Fig. 4.7 (a) to (e). As the enthalpy decreases from the vapor phase, a liquid droplet starts to form, and continues to grow in equilibrium with the vapor environment. Those droplet configurations connect to bubble configurations through a sharp transition before the liquid phase. The occurence of these states agrees with observations in previous work [67, 78, 79]. The structural change of the states along the transition path demonstrates that nucleation is the controlling mechanism of the vapor-liquid phase transition at $P3$.

The configurations of the system at $P7 = 0.096$ are shown in Fig. 4.8. From Fig. 4.8(a) to (f), the system gradually transforms from vapor to liquid phase but stays homogenous without the phase domain separation. At this pressure, the growth of liquid phase takes
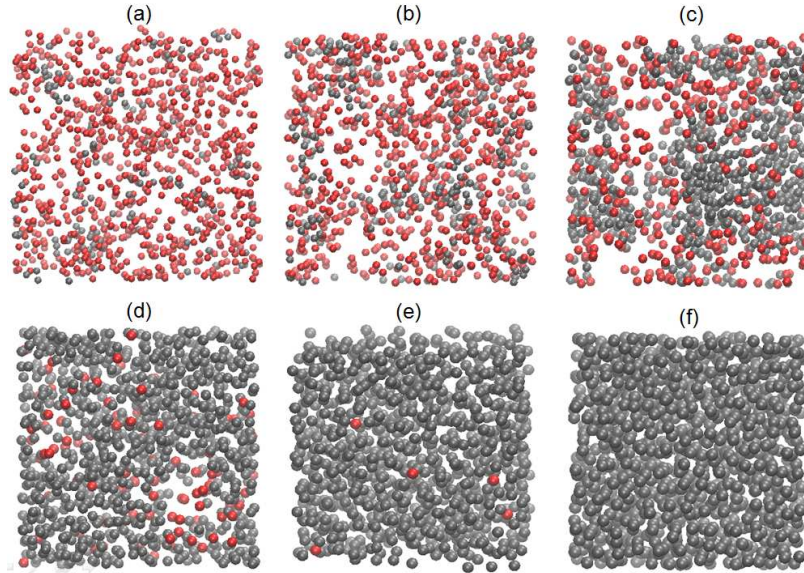
Figure 4.8: Configuration of 6 different states throughout the phase transition at $P7 = 0.096$. The color scheme is the same as in Fig. 4.7. Note that the size of each box is not proportional to the volume of the state.

place in a collective and diffusive manner.

4.4 Conclusion

In this work, we demonstrated the advantages of gREM in simulating the vapor-liquid phase transition in the truncated and shifted Lennard-Jones fluid. The parameterized effective temperatures in gREM are tailored to avoid an intrinsic instability of the canonical ensemble in the negative slope region of the statistical temperature $T_S(H)$ in a first order phase transition. The optimal sampling weight is determined from the effective temperature through the inverse mapping strategy. By combining generalized ensemble sampling with replica exchange, our method enables a comprehensive sampling through phase transition regions with a succession of unimodal enthalpy distributions.

Originally formulatd in the constant volume ensemble, gREM has been extended to the isothermal-isobaric (NPT) ensemble to accomodate the volume change associated with a vapor-liquid phase transition. The phase transition was studied at various pressures be-

low and close to the critical point. The statistical temperature as a function of enthalpy $T_S(H; P)$ is computed at each pressure by ST-WHAM based on the data produced by gREM simulations. The coexisting temperatures and densities are calculated through the Maxwell equal area construction. The spinodal points are identified as the maximum and minimum points of the $T_S(H)$ curves. The phase diagrams in the temperature-density plane and temperature-pressure plane are presented. Our results are consistent with the literature [1] results.

We studied the change in the nature of liquid-vapor phase transition with the change in the pressure. At low pressures, strong first order phase transition features are observed as the backbending in the statistical temperature as a function of enthalpy, $T_s(H)$, and the closed loop in Gibbs function, $G(T)$. However, as the pressure increases, the first-order feature gradually diminishes, and the liquid and vapor phases are connected continuously in the curvature of enthalpy and Gibbs function. The diminishment of the discontinuity indicates that the liquid-vapor transition becomes a second-order continuous phase transition near the critical pressure.

Direct inspection of the atomic configurations of the intermediate states has shown the controlling mechanisms in the two scenarios. At low pressures, it is apparent that nucleation controls the vapor-liquid phase transition as shown by the liquid droplet formation and growth process. Near the critical pressure, a coalescence or collective growth of the new phase displays the characterisic of a second order phase transition.

It is shown that gREM provides insightful observations with the effective sampling for the intermediate states in the vapor-liquid phase transition of a Lennard-Jones fluid. With the intrinsic advantage of sampling first-order phase transition region, gREM will serve as a powerful tool for many systems including complex fluids, and biomolecules.

Chapter 5

Investigating the Solid-Liquid Phase Transition of Water Nanofilms Using the Generalized Replica Exchange Method

5.1   Introduction

Due to its fundamental importance, water has received a great deal of attention in both experimental and computational studies of its complex and often anomolous behavior. Many atomistic models have been built to reproduce the properties of water in molecular simulations using long-ranged forces (electrostatics) which make simulations intrisically computationally demanding. Recently, a coarse-grained monatomic model for water molecules (mW) was developed [80] by Molinero and coworkers to represent water as a single site with three-body potential terms that lead to a tetrahedrality intermediate between carbon and silicon. The mW model captures essential features of the hydrogen-bonding in water using a nonbonded angular dependent term that encourages tetrahedral structure. This potential reproduces the structural, thermodynamic, and dynamic properties of liquid water with comparable or better accuracy to many popular atomistic water models at significantly reduced computational cost. mW has been applied to the study of pure bulk water [81, 82, 83] and nanoconfined water [84, 85, 86], as well as biological water [87] and clathrate hydrates [88].

Nanoscale confined water adds a new dimension of phase behavior and has generated intense interest [89, 90, 84, 86, 91, 92] due to its relevance in biology and materials science. It was reported that the freezing of water encapsulated in a quasi-1D carbon nanotube may occur continuously as well as discontinuously through a first-order phase transition [93]. Recently, the simulation results for water in a quasi-2D hydrophobic nanopore slit also supported the idea that water may freeze by means of both first-order and continuous phase transitions [89]. This is an ideal target as the presence of backbending or a S-loop in the

statistical temperature, determined from gREM, provides a clear indicator of first-order phase transition. We will use gREM to simulate the freezing of bilayer water confined within a slit nanopore and investigate the nature of the liquid-to-solid phase transition with varying densities[1].

5.2 Methods and materials

5.2.1 Monatomic water (mW) model

The monatomic water (mW) [80] potential energy consists of a sum of pairwise two-body (Φ_2) and three-body interactions (Φ_3), parameterized as:

$$E = \sum_i \sum_{j>i} \Phi_2(r_{ij}) + \sum_i \sum_{j \neq i} \sum_{k>j} \Phi_3(r_{ij}, r_{ik}, \theta_{ijk}) \tag{5.1}$$

$$\Phi_2(r_{ij}) = A\epsilon \left[B \left(\frac{\sigma}{r_{ij}} \right)^4 - 1 \right] \exp \left(\frac{\sigma}{r_{ij} - a\sigma} \right) \tag{5.2}$$

$$\Phi_3(r_{ij}, r_{jk}, \theta_{ijk}) = \lambda \sigma (\cos\theta_{ijk} - \cos\theta_0)^2 \exp \left(\frac{\sigma}{r_{ij} - a\sigma} \right) \exp \left(\frac{\sigma}{r_{ik} - a\sigma} \right) \tag{5.3}$$

with $A = 7.049556277$, $b = 0.6022245584$, $\gamma = 1.2$, $a = 1.8$, $\theta_0 = 109.47°$, and the tetrahedrality $\lambda = 23.15$, the diameter $\sigma_{mW} = 2.3925$ Å, and energy scale $\varepsilon = 6.189$ kcal/mol. All intermolecular forces in the mW model vanish at a distance $a\sigma = 4.2$ Å, making the mW model inherently short-ranged and computationally efficient.

In this chapter, the water-like molecules were confined between two parallel featureless hydrophobic plates separated by a distance D. The water-wall interaction was modeled by a Lennard-Jones 9-3 potential as

$$\phi_{\text{LJ-93}} = \epsilon \left[\frac{2}{15} \left(\frac{\sigma_p}{\delta z} \right)^9 - \left(\frac{\sigma_p}{\delta z} \right)^3 \right] \tag{5.4}$$

where δz is the distance in z between the water molecule and the plate, $\sigma_p = 3.56$, and

---

[1]Much of the material presented in this chapter appears in Q. Lu, J. Kim, J. Farrel, D. Wales and J. E. Straub, *Journal of Chemical Physics*, **141**, 18C525 (2014)

$\epsilon = 0.569\,\mathrm{kJ\,mol^{-1}}$ [84].

The separation between plates, D, was chosen to be 8.5Å because the previous study [84] indicated that 8.5 Å is the optimal distance for which the melting temperature of bilayer ice reaches a maximum in the mW model. Periodic boundary conditions were applied in the parallel (x and y) directions to mimic infinite parallel plates. Ten simulations were performed with varying N =256, 576 and 800 water molecules at six different densities ranging from 1.08 g cm^{-3} to 1.23 g cm^{-3}. We have chosen to consider the system at constant volume, following the design of a previous study of phase transitions in nanoconfined water films [89]. The simulation parameters including numbers of particles, lengths of plates, effective densities, effective temperature parameters for gREM, and total simulation times are summarized in Table 5.1, where L_x and L_y are the lengths of the plate in the parallel directions, L_y is fixed to 8.5 Å for all systems, ρ is the effective density, E_0, λ_1, λ_{32} and γ_0 are parameters in T_α. 32 replicas are used in gREM simulations for all systems, and the simulation length is 10^6 MC sweeps. The effective densities are estimated using a method previous described [94] as $\rho = Nm/(L_x L_y L'_z)$, where N is the number of water molecules, m is the mass of a water molecule, and L_x and L_y are the lengths of the plates. Here L'_z is the effective distance accessible to water molecules confined between two hydrophobic plates, defined as $L'_z = D - (\sigma_{\mathrm{mW}} + \sigma_p)/2 = 5.5237$ Å.

5.2.2   Water structure analysis

To characterize structural properties of water molecules the lateral radial distribution function (RDF) $g_{xy}(r)$ [94] is computed as a function of the lateral position r_{xy} parallel to the confining plates as

$$g_{xy}(r) = \frac{1}{\rho^2 V} \sum_{i \neq j} \delta(r - r_{ij}) \left[1 - \theta(|z_i - z_j| - \delta z/2)\right], \tag{5.5}$$

where V is the volume, r_{ij} is the lateral distance between coarse-grained molecules i and j, z is the z coordinate, $\delta z = 2$ Å, and $\delta(x)$ is the Dirac δ function. Note that the Heaviside

Table 5.1: Simulation parameters for 10 systems including number of molecules, plate sizes, effective densities and parameters in gREM.

System	N	L_x (Å)	L_y (Å)	ρ (g/cm³)	E_0 (kJ/mol)	λ_1 (K)	λ_{32} (K)	γ_0 (mol K/kJ)
1	256	36.0	31.2	1.2328	-40.95	220.00	420.00	-36.5679
2	256	34.5	34.5	1.1643	-41.61	200.13	380.25	-18.2764
3	256	34.8	34.8	1.1443	-42.18	200.13	380.25	-14.0019
4	256	35.0	35.0	1.1312	-41.91	200.13	380.25	-15.5259
5	256	35.5	35.5	1.0996	-42.76	200.13	440.29	-22.6551
6	256	35.8	35.8	1.0812	-42.23	200.13	440.29	-24.1468
7	576	56.1	48.6	1.1643	-42.01	220.00	340.00	-4.9615
8	576	57.7	50.0	1.0812	-42.69	240.00	440.00	-10.2134
9	800	61.5	61.5	1.1643	-42.07	220.00	37.000	-5.0381
10	800	63.3	63.3	1.0812	-42.68	220.00	280.00	-5.5218

function $\theta(x)$ restricts the sum to pairs within the same layer.

The lateral static structure factor $S(q)$ is the Fourier transform of the lateral RDF [46, 47] determined as

$$S(q) = 1 + 2\pi\rho \int_0^L r \left(\frac{sin(qr)}{qr} \right) [g_{xy}(r) - 1] dr \qquad (5.6)$$

where $q = 2\pi k/L$, k being an integer number from 1 to N, and L is the length of the simulation box.

5.2.3 Basin-hopping global optimization

Basin-hopping (BH) global optimization [95, 96], as implemented in the `GMIN` package, was employed to explore a simulated potential energy landscape. The BH scheme used in this work is as follows:

1. Apply a random Cartesian displacement to the initial coordinates $\boldsymbol{r}_i$;

2. Find the local minimum $\boldsymbol{r}_n$ from the perturbed coordinates $\boldsymbol{r}_i'$;

3. Accept a trial move to the new configuration $\boldsymbol{r}_n$ with the probability of $p(i \to n) = \min\left[1, e^{-\beta(E_n - E_i)}\right]$ where E_i and E_n are the energies at the initial and new local

minima, and $\beta = 1/kT$.

6×10^3 BH steps were run for each starting structure. At each step, random Cartesian displacements up to 0.8 Å, were applied to each particle. The temperature parameter T was fixed at $8.0\,\mathrm{kJ\,mol^{-1}}$. Local optimization was performed using a modified version of No-cedal's limited memory BFGS (L-BFGS) minimizer[97, 98]. The root-mean-square gradient of the local minima was converged to $10^{-4}\mathrm{kJ/mol/Å}$.

5.3   Results and Discussion

With an optimal choice of effective temperatures $T_\alpha(E; \lambda_\alpha)$ unstable or metastable energy states in the canonical ensemble corresponding to the S-loop region in $T_S(E)$ are transformed into stable states in the generalized ensemble, resulting a unimodal probability distribution function (PDF). The necessary and sufficient condition on $T_\alpha(E; \lambda_\alpha)$ to achieve a unimodal PDF is determined by examining the local stability of the generalized free energy density, $\beta F_\alpha(E) = w_\alpha(E) - S(E)$, at extrema E_α^*, determined as

$$T_\alpha(E_\alpha^*; \lambda_\alpha) = T_S(E_\alpha^*) = T_\alpha^*, \tag{5.7}$$

where E_α^* corresponds to the crossing point between $T_\alpha(E)$ and $T_S(E)$. The stability condition

$$\beta F_\alpha''(E_\alpha^*) = (\gamma_S - \gamma_\alpha)/T_\alpha^{*2}, \tag{5.8}$$

where $\gamma_S = T_S'(E_\alpha^*)$ and $\gamma_\alpha = T_\alpha'(E_\alpha^*)$, the prime being a differentiation with respect to E. Exploiting the linear effective temperatures in Eq. (2.5) a unimodal PDF is ensured by $\gamma_\alpha(E_\alpha^*) = \gamma_0 < \gamma_S(E_\alpha^*)$ around E_α^*. Expanding $P_\alpha(E)$ up to second order at E_α^* verifies

$$P_\alpha(E; \gamma_0) \approx \exp[-(E - E_\alpha^*)^2/2\sigma_\gamma], \tag{5.9}$$

where $\sigma_\gamma = T_\alpha^{*2}/(\gamma_S - \gamma_0)$, yielding a Gaussian PDF centered at E_α^*.
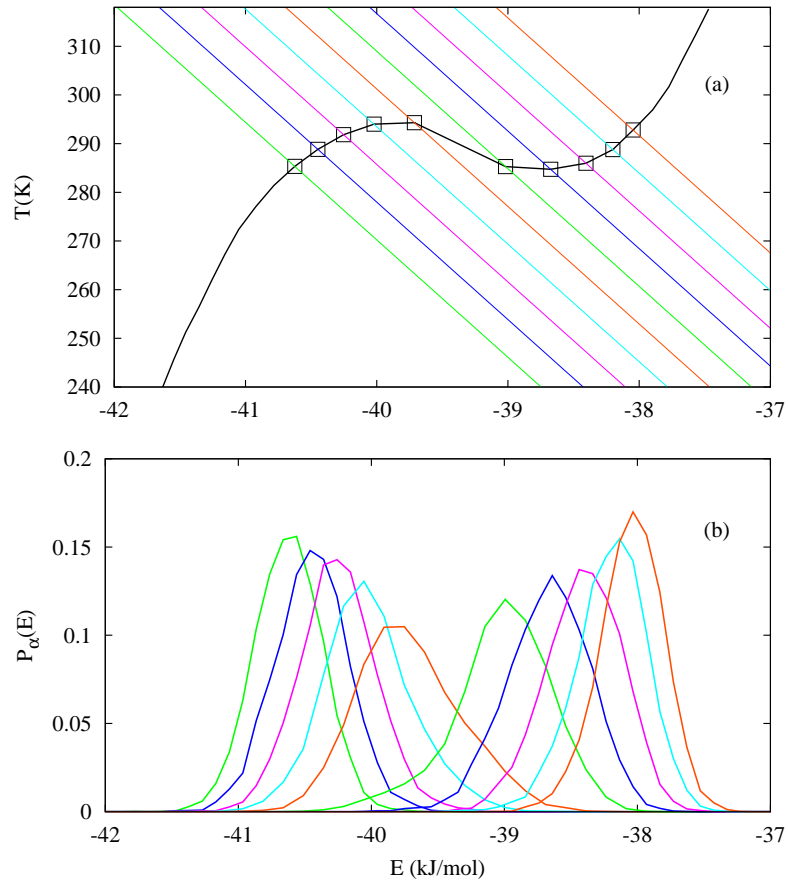
Figure 5.1: (a) Effective temperatures $T_\alpha(E)$ (a set of parallel lines with negative slope) form unique crossing points (black open squares) with the statistical temperature $T_S(E)$ (black curve), (b) generalized probability distributions functions $P_\alpha(E)$ of corresponding replicas $\alpha = 17, 18, 19, ..., 26$ of system 6 in Table 5.1.

Fig. 5.1a demonstrates that the linear effective temperatures $T_\alpha(E)$ form unique crossing points E_α^* with the statistical temperature $T_S(E)$ across the transition region, where $T_S(E)$ displays the S-loop. Setting $E_0 = -42.23\,\mathrm{kJ\,mol^{-1}}$ and $\gamma_0 = -24.15\,\mathrm{mol\,K\,kJ^{-1}}$ replica-dependent effective temperatures, $T_\alpha(E; \lambda_\alpha) = \lambda_\alpha + \gamma_0(E - E_0)$, were assigned using evenly spaced λ_α between $\lambda_1 = 200.13\,\mathrm{K}$ and $\lambda_{32} = 440.29\,\mathrm{K}$. As illustrated in Fig. 5.1b the linear effective temperatures with negative slope, $\gamma_0 < \gamma_S(E_\alpha^*)$, result in $P_\alpha(E)$ centered at E_α^* with a Gaussian shape, naturally bridging between ordered and disordered phases with unimodal energy distributions across the transition region. Figs. 5.1 through 5.3 show simulation

results of System 6 in Table 5.1.
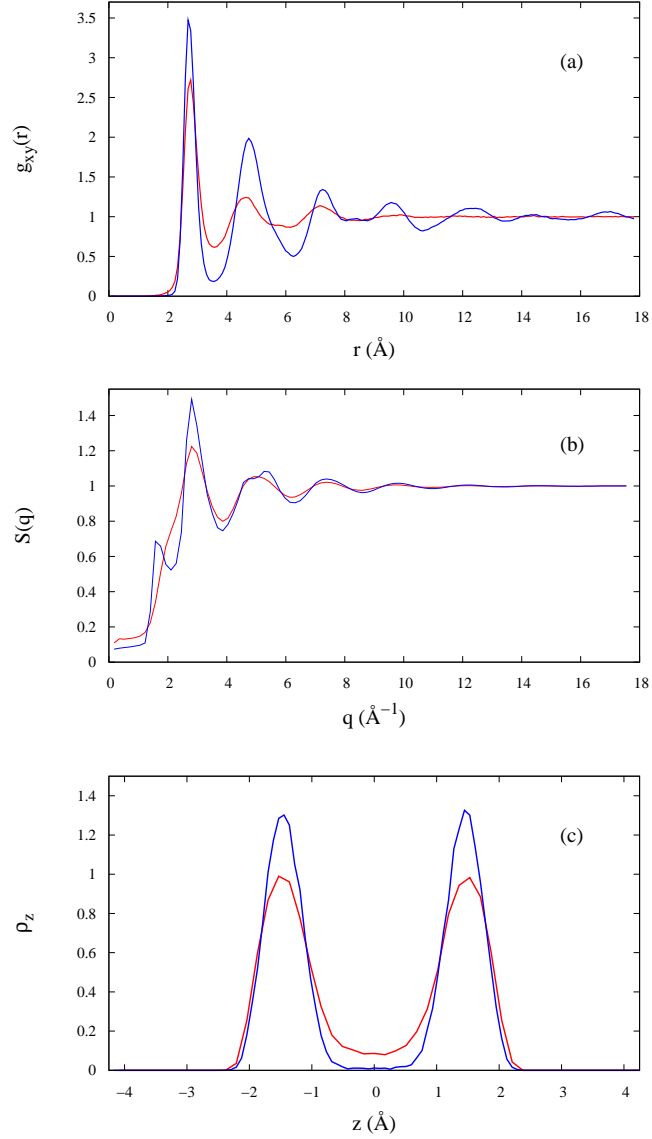
Figure 5.2: (a) Lateral radial distribution function $g_{xy}(r)$ and (b) structure factor transformed from $g_{xy}(r)$ of replica 18 (blue line) and replica 25 (red line) of the same systems as in Fig.1. (c) The transverse density profile of water along confinement direction (z direction) for replica 18 (blue) and replica 25 (red).

In order to characterize structural differences between liquid and solid phase near the transition temperature, we compared the lateral radial distribution functions $g_{xy}(r)$ (RDF)

and structure factors $S(q)$ of two representative replicas corresponding to replica 18 and 25 (see Fig. 5.2). Note that the effective temperatures, $T_{18}(E)$ and $T_{25}(E)$, form crossing points with $T_S(E)$ at E_{18}^*=-40.45 kJ/mol and E_{25}^*=-38.20 kJ/mol, respectively, at the same $T_{18}^* = T_{25}^* = 288.7$ K. The RDFs of replica 18 and 25 in Fig. 5.2a show marked differences in terms of the magnitude of the peaks, and the number of peaks. The RDF of replica 18 corresponding to the solid phase has several pronounced peaks up to 14 Å, while only three peaks are visible in replica 25, indicating an absence of long-range orders characteristic to the liquid phase. The structure factor of replica 18 displays a prepeak at $q \approx 2$, a sharp first peak, and a split second peak, while $S(q)$ in replica 25 lacks the prepeak and and the split in the second peak.

To examine the layering effects from confinement, we computed the transverse density profile ρ_z (TDP) along the z direction in Fig. 5.2c. Both TDPs at replicas 18 and 25 have two pronounced symmetric peaks with respect to the slit center ($z = 0$), confirming that two layers of water molecules are confined in the nanoslit. However, the TDP in replica 25 has a significant wider distribution with smaller peaks at each layer center and with non-zero density values across the slit center, while the TDP of replica 18 shows a vanishing density at the slit center. This implies that water molecules in replica 25 can easily move between two layers across the slit center, while transverse movements of water molecules in replica 18 are highly restricted, resulting in a strong layering effect. The differences in RDFs, structure factors, and transverse density profiles reveal the solid-like and liquid-like characteristics of the configurations in replicas 18 and 25, respectively, manifesting the coexistence of two structurally distinct states in the canonical ensemble.

After a sufficiently long simulation with gREM, multiple replica simulations are optimally combined to produce the entropy estimate, $S(E)$, via ST-WHAM. Once the entropy is determined, canonical thermodynamic properties including internal energy $E(T)$ and heat capacity $C_v(T)$, can be calculated as in Eq. (2.12) and (2.13). In contrast to the statistical temperature $T_S(E)$ characteristic to microcanonical ensemble in Fig. 5.1a, the canonical
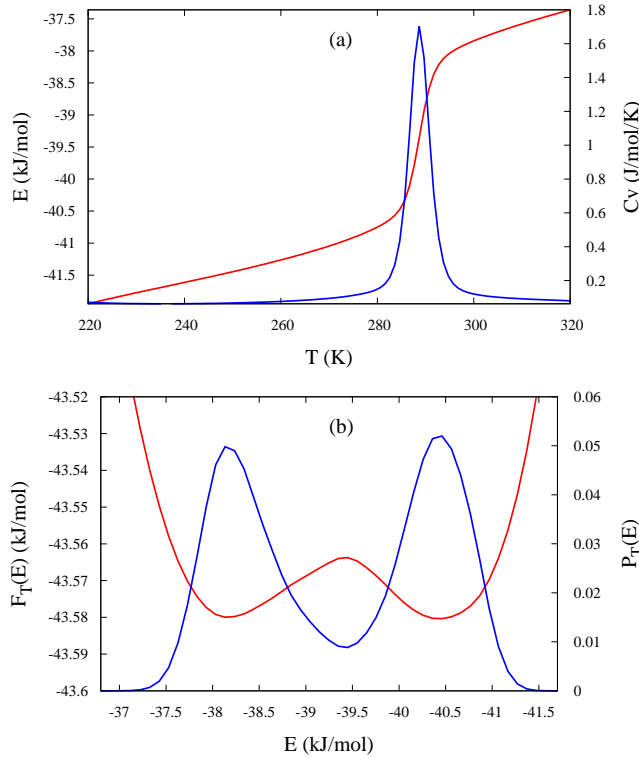
Figure 5.3: (a) Energy temperature curve in the canonical ensemble (red line) and molar heat capacity $C_v(T)$ (blue line) of system 6. (b) Probability distribution function $P_T(E)$ (blue) and free energy $F_T(E)$ (red) at the melting temperature T_m=288.7 K.

ensemble average, $E(T)$, monotonically decreases with T and shows a sharp drop across the phase transition region in Fig. 5.3a, which is corresponding to the peak in the heat capacity C_v around the transition temperature $T_m \approx 288.7$K. The free energy density in Fig. 5.3b at T_m, $F(E, T_m) = E - T_m S(E)$, exhibits two local minima at $E_1 = -38.1$ and $E_3 = -40.5 \, \text{kJ} \, \text{mol}^{-1}$, and one local maximum at $E_2 = -39.5 \, \text{kJ} \, \text{mol}^{-1}$, resulting in the bimodal structure in $P_T(E)$ in contrast to the unimodal PDFs in gREM across the phase transition region [30, 31, 32, 33].

We also performed several gREM simulations as a function of density, ρ, with varying system size $N = 256$, 576, and 800 (see Table 5.1 for the detailed description of systems) to explore the effect of density on the phase transition in nanoconfined mW water. The
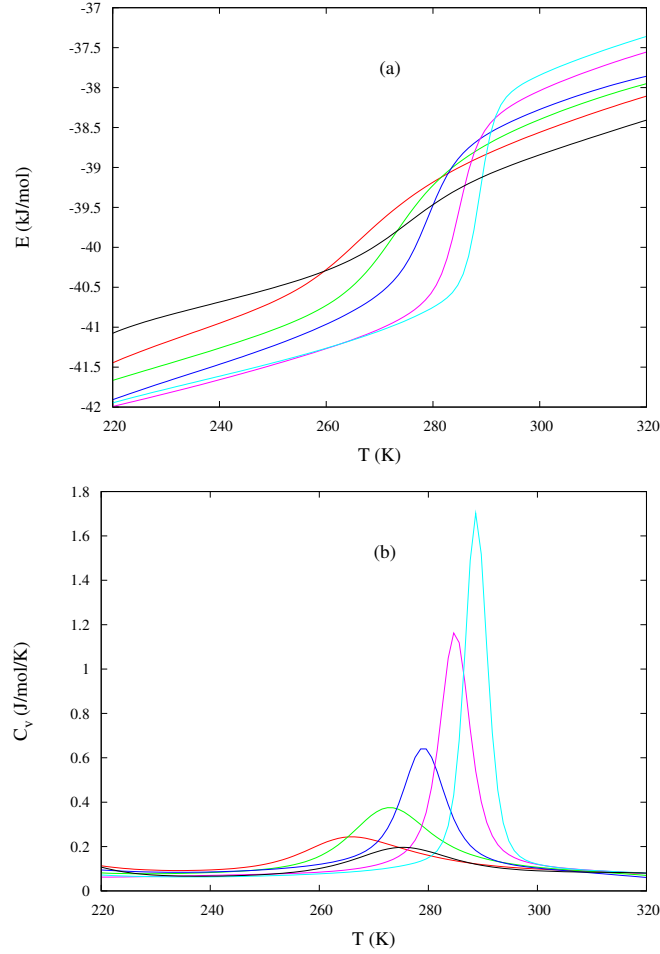
Figure 5.4: (a) Energy versus temperature curve, E(T), and (b) Molar heat capacity, $C_v(T)$, of System 1 to System 6, the parameters of which are given in Table 5.1.

reweighted internal energies and heat capacities in the canonical ensemble for System 1 through System 6 were illustrated in Figs. 5.4 (a) and 5.4 (b), respectively. Interestingly, the magnitude of the drop in the internal energy (latent heat) across the transition region from liquid to solid is monotonically decreasing as ρ decreases, which is accompanied by a sharp drop in the magnitude of the peak in the heat capacity. This demonstrates that the first-order character of the phase transition between liquid and solid in nanoconfined mW water becomes much weaker in the high density regime, in which freezing of water may occur through a continuous transformation.
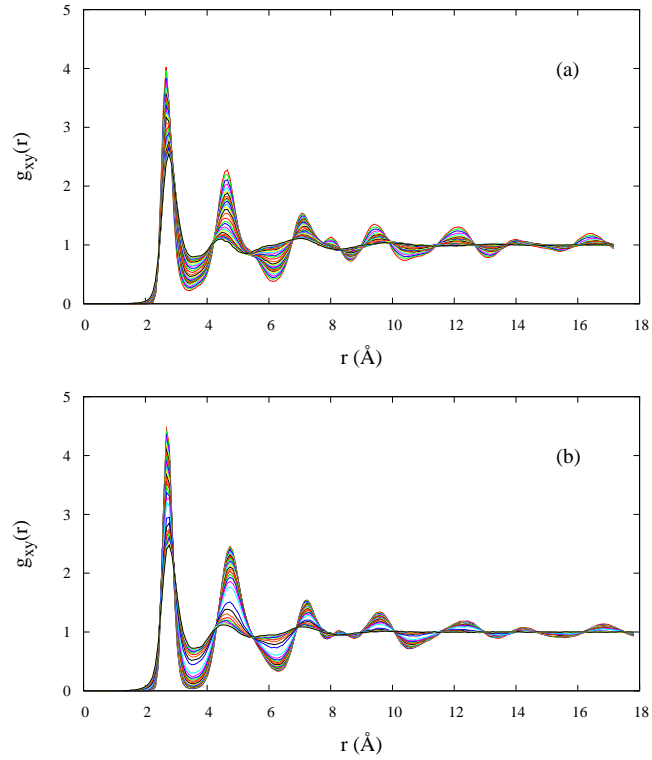
Figure 5.5: Lateral radial distribution function $g_{xy}(r)$ of all replicas in system 2 (a) and system 6 (b).

To investigate structural changes associated with the phase transition at various ρ, both profiles of the RDF and TDP are examined across replicas near the transition region for System 2 and 6 corresponding to $\rho = 1.0812$ g cm^{-3} and 1.1643 g cm^{-3}, respectively. As illustrated in Fig. 5.5a, the variation of $g_{xy}(r)$ at high density is almost continuous across replicas, while at low density $g_{xy}(r)$ is well segregated as can be seen in the first and second peaks in Fig. 5.5b. The continuous variation of $g_{xy}(r)$ at higher density is most apparent in the long-range order. For the lower density system, there are clearly two sets of replicas - those that show substantial long-range order and those that do not - with an abrupt transition between the two. The substantial differences in the behavior of $g_{xy}(r)$ for the high and low density systems are also apparent in the transverse density profiles in Figs. 5.6 (a) and (b). At higher density (System 2), the peaks for the center of each layer center are

continuously rising across replicas from liquid to solid with a marginal density at the slit center. This indicates that transverse movements of waters is highly restricted in both solid and liquid phase. At lower density (System 6), the profiles show higher non-zero density at the slit center in liquid phase replicas, implying that water molecules can freely move between the two layers in the liquid phase.
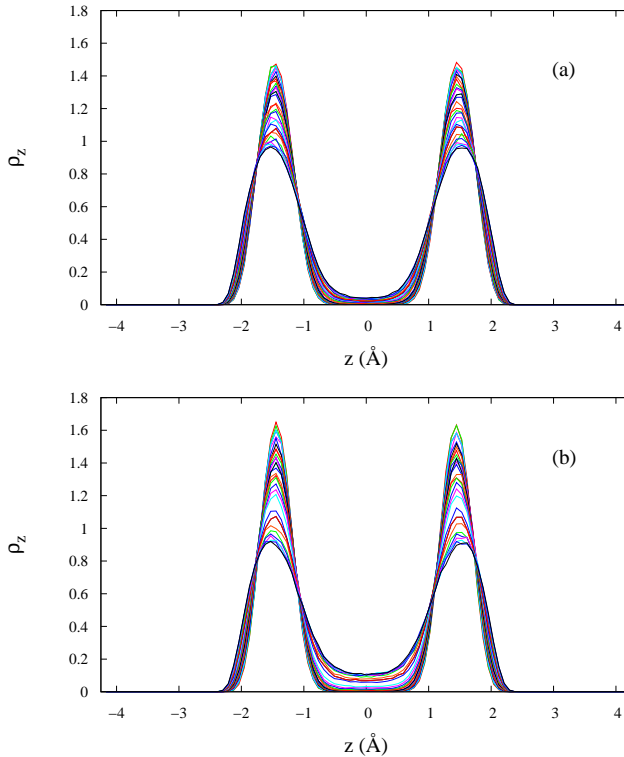
Figure 5.6: The transverse density profiles (TDP) of water along confinement direction (z direction) of all replicas in system 2 (a) and system 6 (b).

These observations are consistent with the Stanley group's conjecture regarding the possibility of a "crossover" from first-order to continuous transition between the liquid and solid states with increasing density [89]. We note that this crossover behavior was not observed in previous work by Molinero and coworkers [86]. However, that work was based on a $NP_{xy}T$ ensemble, while we have used an NVT ensemble, as was done in the study of the Stanley group [89]. The Stanley group also did note crossover behavior in an $NP_{xy}T$

ensemble simulation as well [89].
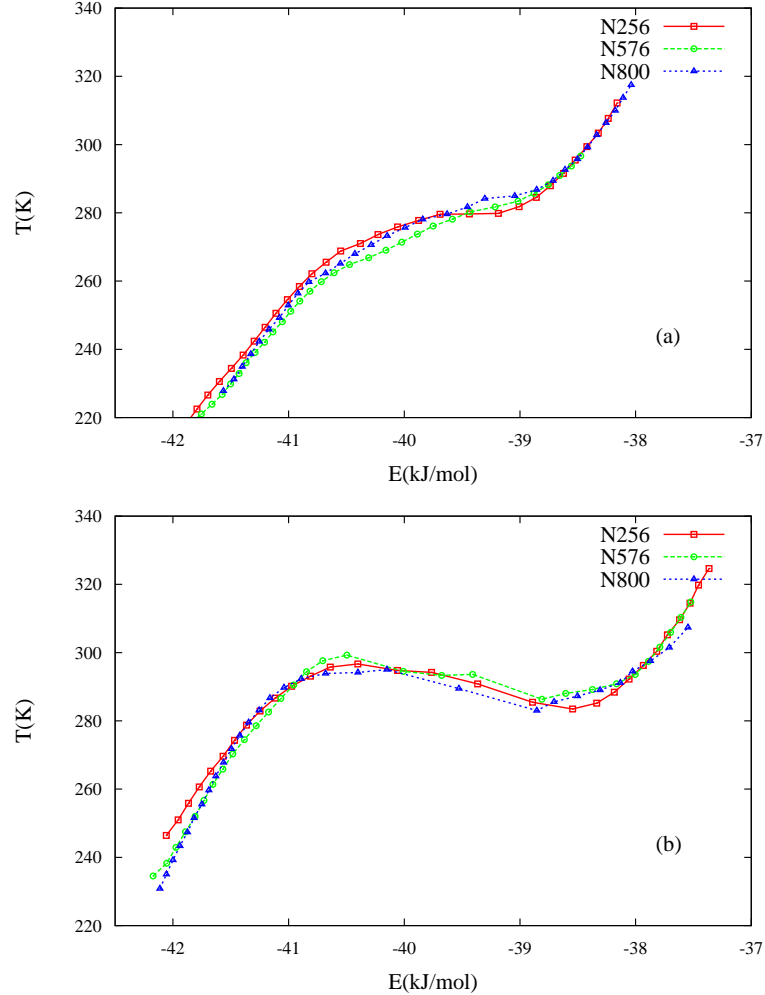
Figure 5.7: The energy temperature curves formed by most probable energy sets $[E_\alpha^*, T_\alpha^*]$ determined by gREM simulations for systems with densities $\rho_1 = 1.1643\mathrm{gcm}^{-3}$ (a) and $\rho_2 = 1.0812\mathrm{gcm}^{-3}$ (b). The lines and symbols in red, green and blue show the results for systems with 256, 576 and 800 molecules, respectively.

The crossover behavior from a first-order to continuous transition with increasing density is also seen in the profile of the approximate statistical temperatures, $T_S(E)$, in Fig. 5.7, in which the most probable energies E_α^*, corresponding to the crossing points between $T_\alpha(E)$ and $T_S(E)$, were plotted with $T_\alpha^* = T_\alpha(E_\alpha^*; \lambda_\alpha)$ across replicas for $N = 256$, 576 and 800, while maintaining the density of systems at $\rho_1 = 1.1643\mathrm{gcm}^{-3}$ in Fig. 5.7a and

$\rho_2 = 1.0812\text{gcm}^{-3}$ in Fig. 5.7b. We found that the statistical temperature estimates from several independent gREM simulations at different N are in overall good agreement, implying that finite size effects are marginal in our simulations. Interestingly, $T_S(E)$ for low density systems shows a clear S-loop, characteristic to first-order phase transitions, while it varies monotonically without noticeable structures across the transition region in high density systems.
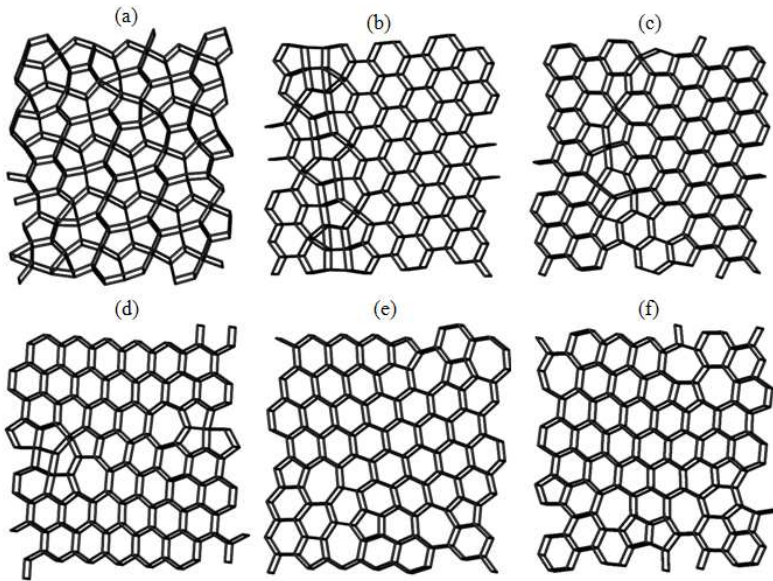
Figure 5.8: (a) to (f) show the minimized structures of systems 1 to 6, respectively.

To characterize the globall minima structures for System 1 through 10, basin-hopping global optimization (BH) [99, 100, 101] was applied starting from equilibrium configurations of the lowest replica in each gREM simulation using the GMIN package, yielding representative snap shots in Figs. 5.8 and 5.9. The putative global minimum of System 8 at $\rho = 1.0812$ g cm^{-3} for $N = 576$ corresponds to a regular hexagonal ice form, while in all other systems the ground states were imperfect hexagonal ices with defects. While this leads to a less regular global minimum structure, our results show that it does not impact the character of the thermodynamics of the solid-to-liquid phase change. The minimized structures for these systems have different composition of polygonal rings in each layer. We made use of graph

representations of the structures, in which vertices represent particles, and an edge between two vertices represents a nearest neighbor contact between two particles with a cut-off of 3.35 Å. A ring is a connected graph in which each vertex shares exactly two edges with other vertices in the ring. For the bilayer structures in this work, we counted rings within individual layers. We calculated a composition of $n-$membered rings on the basis of 100 minimized structures.
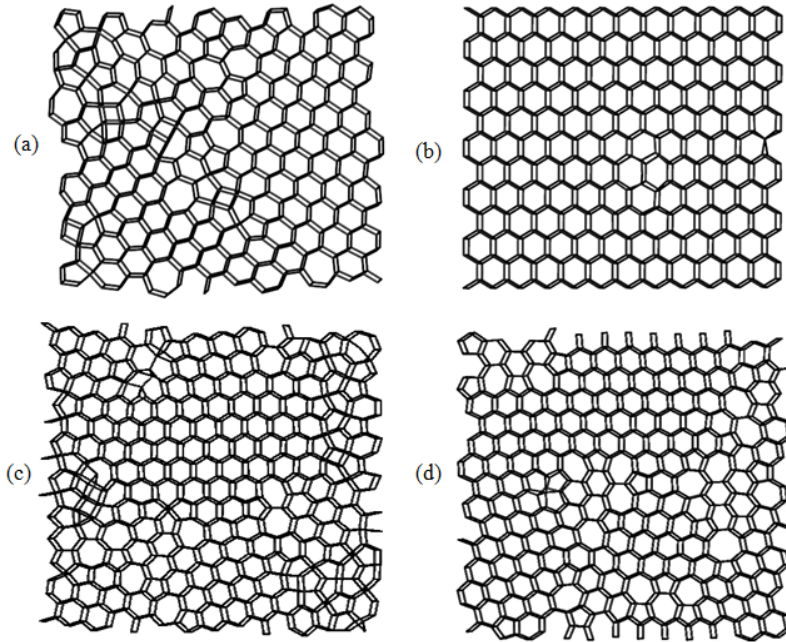
Figure 5.9: (a) to (d) show the minimized structures of systems 7 to 10, respectively.

Table 5.2 lists the percentage distributions of n-membered rings ($n = 4, 5, 6, 7$) for System 1 to 10, showing an overall trend that the composition of pentagonal rings drops with decreasing density and the composition of hexagonal and heptagonal rings increases with decreasing density.

5.4   Conclusion

In summary, the effectiveness of the generalized replica exchange method (gREM) for first-order phase transitions was demonstrated using nanoconfined monatomic water (mW) sys-

Table 5.2: Percentage distributions of the $n-$membered ring in system 1 to 10.

ring size	n=4 (%)	n=5 (%)	n=6 (%)	n=7 (%)
System 1	0.47	93.32	6.21	0
System 2	3.15	25.92	68.94	1.99
System 3	2.34	15.83	77.13	4.70
System 4	2.64	14.58	78.57	4.22
System 5	0.10	13.42	73.50	12.99
System 6	1.22	17.84	65.76	15.17
System 7	3.36	25.75	63.90	6.98
System 8	0.03	2.77	95.23	1.97
System 9	2.84	35.07	55.29	6.80
System 10	0.09	12.75	75.96	11.20

tems at diverse simulation conditions. Combined with efficient replica exchanges across unimodal energy distributions spanning phase transition regions, gREM attains a comprehensive sampling for metastable and unstable configurations intrinsic to the phase transitions, which are rarely accessed in canonical ensemble simulations due to the need to overcome a substantial free energy barrier.

With an optimal integration of multiple replica simulations of gREM using the statistical temperature weighted histogram analysis method (ST-WHAM), we investigated detailed thermodynamic and structural properties of solid-liquid phase transitions in nanoconfined mW water at various densities. The first-order phase transitions between liquid and hexagonal ice in the low density regime was explicitly illustrated in terms of the existence of S-loop or backbending in the statistical temperature $T_S(E)$, sharp drops in internal energies, pronounced peaks in heat capacities, and quantitative differences in profiles of lateral radial distribution functions (RDF) and transverse density profiles (TDP) between solid and liquid phases. Interestingly, it was found that the first-order transition character in nanoconfined mW water is weaker at high density, accompanied by an absence of backbending character in $T_S(E)$, gradual changes of both internal energies and heat capacities, and continuous variations of both RDFs and TDPs across replicas in phase transition regions. These observations support the conjecture of a crossover from the first-order to continuous

transition in quasi-two-dimensional confined water systems with increasing density, which was recently hypothesized based on full atomistic simulations of a TIP5P water [89].

The graph representation analysis for low-lying solid-phase structures, determined by basin-hopping global optimization using the GMIN package, shows heterogeneous crystalline structures composed of different compositions of pentagonal, hexagonal, and heptagonal rings depending on the simulation conditions. Interestingly, minimized structures of low density systems exhibiting the first-order transition character contained dominant hexagonal rings, while the composition of pentagonal rings gradually increases in high density systems showing continuous transitions.

Chapter 6

Phase Transitions of Coarse-Grained Water Confined between Plates of Different Affinities and Separations

6.1   Introduction

Confined water is present in biological systems and nanoscale materials, and is known to possess a variety of structural, dynamic and thermodynamic properties that differ from bulk water [89, 90, 84, 85, 86, 91]. These are direct results of the interaction with surfaces and/or a truncation of the bulk correlation length, and depend on the detailed interactions of water with the interfacial particles, which may be hydrophilic or hydrophobic in nature [94]. Moreover, the geometry of the confinement is also an important factor. Cylindrical nanopores and parallel slit nanopores are two types of confining geometries used in studies of nanoconfined water [89, 90, 84, 85].

This chapter focuses on bilayer water confined to a slit nanopore made of two infinite parallel plates separated by a fixed distance. Previously, we have simulated the solid-to-liquid phase transition in bilayer water as a function of density, demonstrating a variation in the order of the transition from first (at low densities) to second (at high densities). The focus of this study is to probe the effect of varying hydrophilicity of the plates and the plate-to-plate distance on the thermodynamic and structural properties of the nanoconfined water film.

Due to the large latent heat associated with the solid-to-liquid phase transition in water nanofilms, it is hard to precisely determine the phase transition temperature and other thermodynamic properties using regular MD simulations in canonical ensembles. As such, it is of interest to explore the phase behavior using a generalized ensemble approach.

In this chapter, we employed the gREM to simulate the solid-to-liquid phase transition

of coarse grained mW water nanofilm. Our results suggest a remarkable sensitivity of the transition to the nature of the water-wall interaction, with implications for understanding interfacial and nano-confined water.

6.2 Methods and materials

6.2.1 Water-water and water-plate interactions

The interactions between water-water molecules are modeled by the mW potential [80], which consists a sum of pairwise two-body and three-body interactions described by a functional form of the Stillinger-Weber potential [102] as shown in Eq. (5.3). The Stillinger-Weber potential was originally developed to model silicon. Only three parameters are changed to adapt the silicon model to the mW model, which are the tetrahedrality $\lambda = 23.15$, the diameter $\sigma_{\mathrm{mW}} = 2.3925$ Å, and energy scale $\epsilon = 25.895$ kJ/mol.

We investigate the state of water confined between both hydrophilic and hydrophobic plates. The water-plate interaction was modeled following prior studies [84]. The simulation results of water in cylindrical nanopore using this water-wall potential were comparable with the experimental results of water in silica nanopore [84]. One plate consists of particles arranged in a single-layer triangle lattice with interparticle spacing 3.2 Å. The interactions between water molecules and particles on the plates were modeled with the two-body potential in Eq. (5.3) with σ_{wp} set to 3.2 Å to prevent the diffusion of water molecules into the plate, $\varepsilon_{\mathrm{wp}}$ modulating the hydrophilicity of the plate, and other constants for the water-plate interactions chosen to be the same as those for water-water interactions in the mW model. As the plate-water interaction does not have a three-body potential in this work, the plates do not form directional hydrogen bonds with the water molecules. The hydrophilicity of the plates was characterized by Molinero and coworkers [85] by the simulation of the contact angle of droplets with a flat plate. On the basis of their results, we set the parameters of two hydrophobic plates to be $\varepsilon_{\mathrm{wp}}$=0.2 and 0.3 kcal/mol and the parameters of two hydrophilic plates to be $\varepsilon_{\mathrm{wp}}$=0.5 and 0.7 kcal/mol.

6.2.2   Systems

The water nanofilm systems are composed of 256 water molecules confined between two parallel plates separated by a distance D, varying between 8 and 10 Å, with 0.5 Å as the interval. Distances in this study are measured from the centers of the plates. The plate-water interactions are governed by Eq. (5.3.2), in which $\varepsilon_{\mathrm{wp}}$ modulates the hydrophilicity of the plates. We simulated two hydrophobic plates with $\varepsilon_{\mathrm{wp}}$=0.2 and 0.3 kcal/mol, and two hydrophilic plates with $\varepsilon_{\mathrm{wp}}$=0.5 and 0.7 kcal/mol. The system is periodically replicated in the x and y directions to model confinement between infinite plates. The lateral pressures of water nanofilms are maintained at 1 atm. The lateral dimensions of the water nanofilm are allowed to fluctuate while the interplate distance is fixed at a certain distance.

6.3   Results and Discussion

6.3.1   Thermodynamic properties

We simulated 20 systems of 5 different interplate distances, D=8, 8.5, 9, 9.5, 10 Å, and 4 different water-plate interaction strengths, $\varepsilon_{\mathrm{wp}}$=0.2, 0.3, 0.5 and 0.7 kcal/mol. The aim is to carry out an extensive study of the effect of the hydrophilicity of the plates and the plate-to-plate distance on the thermodynamic and structural properties of water nanofilms. Simulations of the solid-to-liquid transition in water nanofilms were performed using gREM. ST-WHAM was used to determine the entropy estimate, $S(H)$, and the stastistical temperature, $T_{\mathrm{S}}(H)$, which is determined through $T_{\mathrm{S}}(H) = (\partial S(H)/\partial H)^{-1}$. The canonical expectaction value for the enthalpy and the isobaric heat capacity are computed using Eq.(2.12) and (2.13). The solid-to-liquid phase transition temperature was determined as the maximum of the heat capacity. Changes in enthalpy, entropy, and volume of the transition were also computed.

Fig. 6.1 shows the statistical temperature and the canonical temperature of the system with D=9 Å and $\varepsilon_{\mathrm{wp}}$=0.2 kcal/mol. The statistical temperature shows backbending behav-
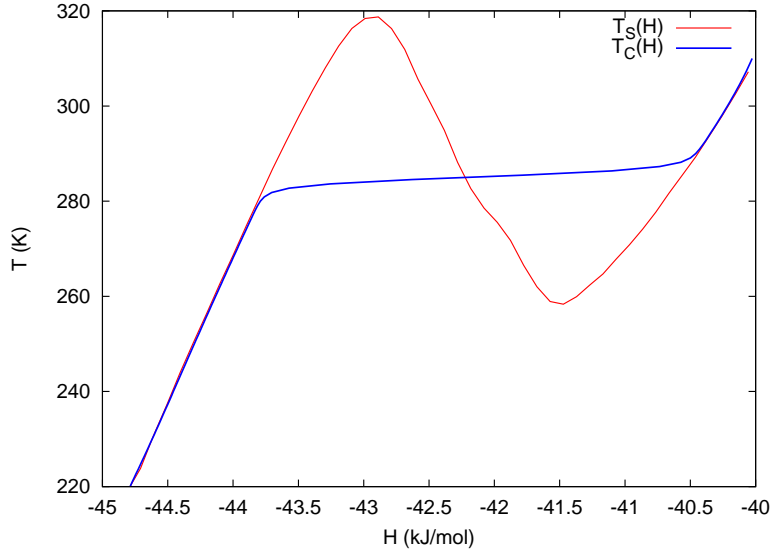
Figure 6.1: The statistical temperature, $T_S(H)$, and the canonical temperature, $T_C(H)$, of the system with $D=9$ Å and $\varepsilon_{wp} = 0.2$ kcal/mol, plotted as red and blue lines, respectively.

ior as an indicator of the strong first order solid-to-liquid phase transition. In gREM, the S-loop is removed when the temperature is reweighted into the canonical ensemble. The canonical temperature is monotonically increasing as a function of enthalpy in the canonical ensemble.

Fig. 6.2 shows the enthalpy-temperature curves, H(T), and the isobaric heat capacity, $C_p(T)$, of the systems with interplate distance $D=8$ Å and 10 Å and four different water-plate interaction strengths, ε_{wp}=0.2, 0.3, 0.5 and 0.7 kcal/mol. In all cases, a sharp peak in $C_p(T)$ and discontinuous changes in $H(T)$ are observed, suggesting a first-order phase transition. The enthalpy curve moves downwards as ε_{wp} increases, indicating the enthalpy of both ice and liquid phases decreases as ε_{wp} increases. At the same time, the enthalpy curve and the heat capacity curve shift to the right as ε_{wp} increases, indicating the transition temperature increases as ε_{wp} increases. For systems with $D=8$ Å, the peaks in $C_p(T)$ are approximately of the same heights for different values of ε_{wp}. For systems with $D=10$ Å, the height of the peak in $C_p(T)$ increases as ε_{wp} increases, indicating that the phase transition
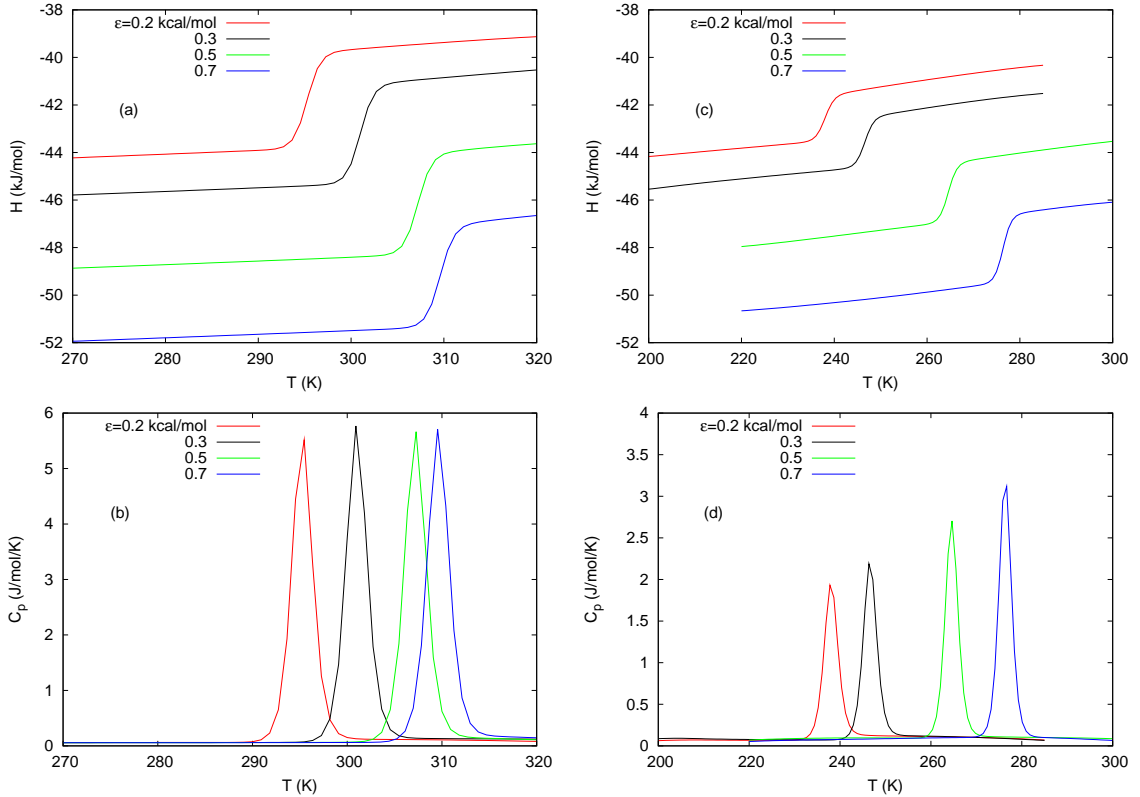
Figure 6.2: (a) Enthalpy, $H(T)$ and (b) isobaric heat capacity, $C_p(T)$, in canonical ensembles for systems with D=8 Å and ε_{wp}=0.2, 0.3, 0.5 and 0.7 kcal/mol. (c) Enthalpy, $H(T)$ and (d) isobaric heat capacity, $C_p(T)$, in canonical ensembles for systems with D=10 Å and ε_{wp}=0.2, 0.3, 0.5 and 0.7 kcal/mol.

becomes stronger as the water-plate interaction becomes more hydrophilic.

From the location of the peaks of the isobaric heat capacity curves, the solid-to-liquid phase transition temperatures of all 20 systems were determined. The transition temperatures as a function of the interplate distance D are shown in Fig. 6.3 for systems with ε_{wp}=0.2, 0.3, 0.5 and 0.7 kcal/mol. The transition temperature reaches a maximum at D=8.5 Å at all values of ε_{wp}, and is observed to decrease as the interplate distance increases from 8.5 Å to 10 Å. The parabolic behavior of the transition temperatures near D=8.5 Å agrees with previous observations [84]. At a given value D, the transition temperature is higher when ε_{wp} of the system is larger. Varying both parameters for interplate distance and
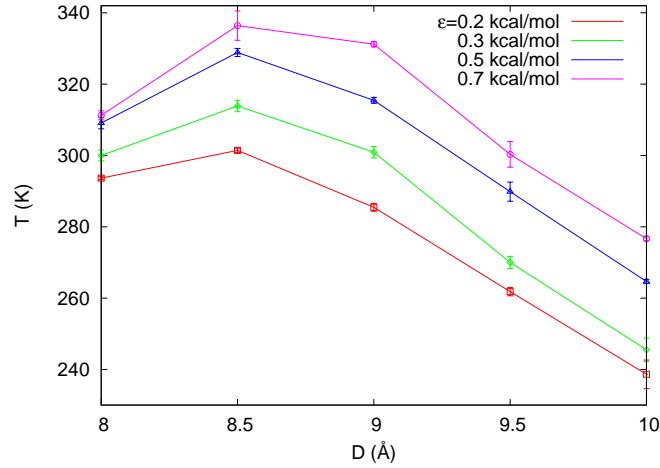
Figure 6.3: The phase transition temperature of water nanofilms at interplate distance D=8, 8.5, 9, 9.5 and 10 Å for systems with four different plate-water interation parameters, ε_{wp}=0.2, 0.3, 0.5 and 0.7 kcal/mol.

the water-plate interaction, D and $\varepsilon_{\mathrm{wp}}$, the transition temperature of the water nanofilm is observed to span over a wide range from 240 K to 340 K.

Fig. 6.4 shows the change in enthalpy, ΔH, and entropy, ΔS, for the solid-to-liquid transition for different interplate distances D, for both a hydrophobic plate ($\varepsilon_{\mathrm{wp}}$=0.2 kcal/mol) and a hydrophilic plate ($\varepsilon_{\mathrm{wp}}$=0.7 kcal/mol). At all distances, within the statistical error, the change in enthalpy for systems with hydrophilic plates are higher than for the corresponding systems with hydrophobic plates. This results from the fact that water-plate interaction is more favorable than the water-water interaction, leading to an expansion in the liquid state. For systems with hydrophobic and hydrophilic plates, as D increases from 8 to 9.5 Å, ΔH, and ΔS are observed to decrease monotonically. This results from the fact that as D increases, the solid state becomes less structured with higher potential energy and entropy, while the liquid state is relatively more condensed and ordered. For systems with strong hydrophilic plates, the results at D=10 Å do not follow that same trend as ΔS increase, and ΔH maintains a constant value. This is the apparent result of a substantial structural change in the water nanofilm as D increases to 10 Å (discussed below).
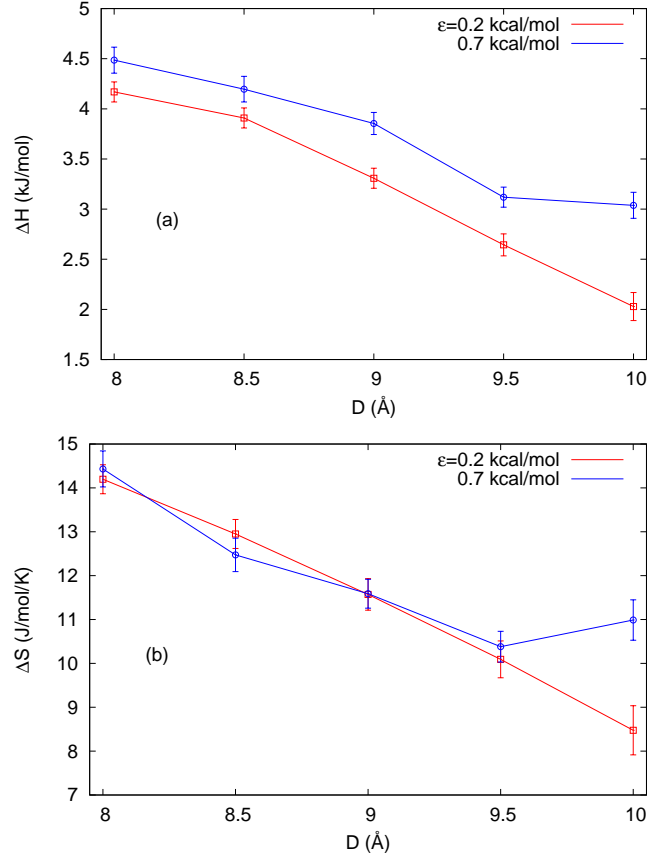
Figure 6.4: (a) - (c) Change in enthalpy ΔH, and entropy ΔS, for the solid-to-liquid transition in water nanofilms with varying interplate distances, D, for a hydrophobic plate (ε_{wp}=0.2 kcal/mol) and a hydrophilic plate (ε_{wp}=0.7 kcal/mol).

6.3.2   Structural properties of nanonconfined waterfilm

Structural layering effects induced in the water nanofilm by confinement are examined through the transverse density profile, ρ_z, (TDP) along the direction z, for ice structures of all 20 systems at T=220 K (see Fig. 6.5). The zero point of the z-axis is defined as the midpoint between the two plates. The profiles of ρ_z show two peaks symmetric with respect to the midpoint between the plates with interplate distance D=8, 8.5, 9 and 9.5 Å, indicating two layers of water molecules confined between plates. When D=8, 8.5, 9 and 9.5 Å, the peaks in ρ_z assume a gaussian-like shape centered around z=$\pm$1.4 Å, indicating both layers are flat (consistent with the 2B structure in Ref. [84]). Meanwhile, the height

of the peaks diminishes as D increases from 8 to 9.5 Å, reflecting weaker confinement of the bilayer. Correspondingly, for the same interplate distance, the height of the peaks increases with increasing ε_{wp}.
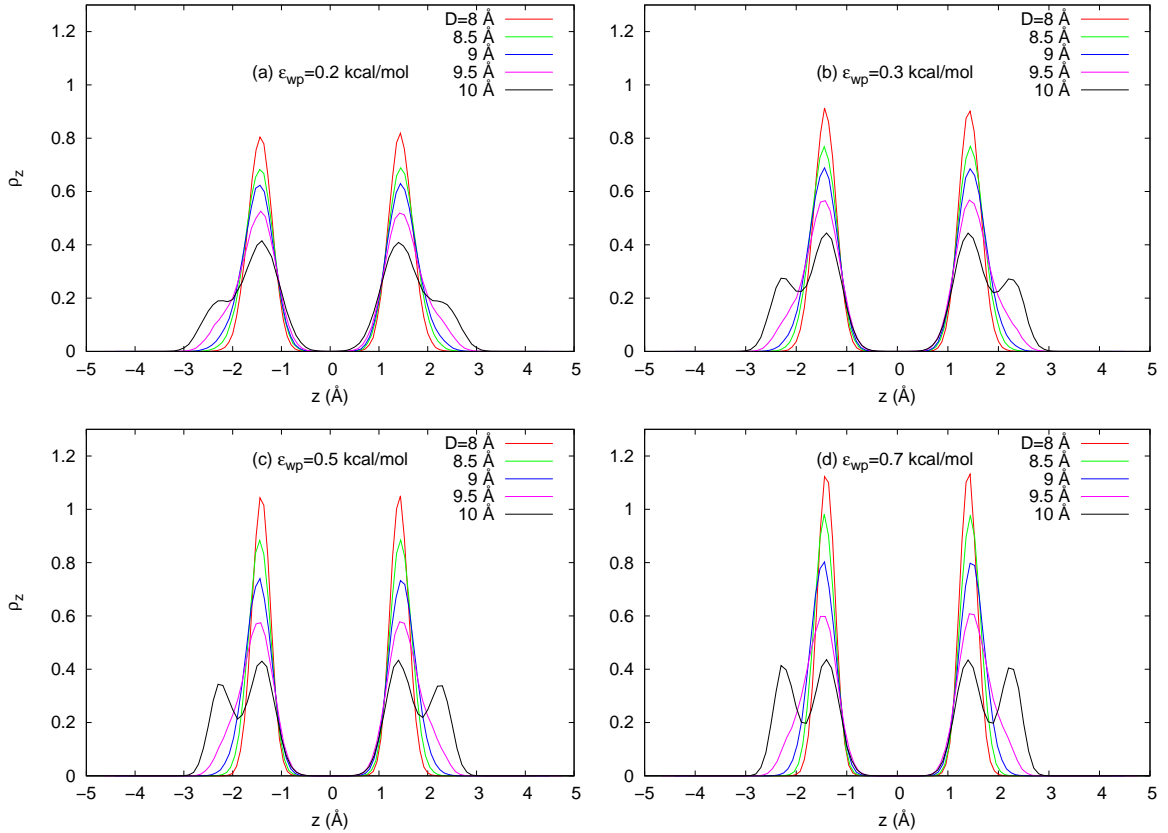
Figure 6.5: (a)-(d) The transverse density profiles, ρ_z, of systems with four different water-plate interaction parameters, ε_{wp}=0.2, 0.3, 0.5 and 0.7 kcal. Each subfigure compares ρ_z of systems with varying interplate distances D=8, 8.5, 9, 9.5, 10 Å, but the same water-plate interaction parameter, ε_{wp}.

The profiles of ρ_z become different as D increases to 10 Å. When D=10 Å and ε_{wp}=0.2 kcal/mol, each of the main peaks in ρ_z shows a shoulder around z=±2.3 Å. The shoulder grows into a subpeak when ε_{wp}=0.3 kcal/mol and D=10 Å. The height of the subpeak continues to grow as ε_{wp} increases to 0.5 and 0.7 kcal/mol, while the location of the subpeak remains the same. When D=10 Å and ε_{wp}=0.7 kcal/mol, the heights of the subpeaks are equivalent to the heights of the main peaks, which are located at z=±1.4 Å. The split of each
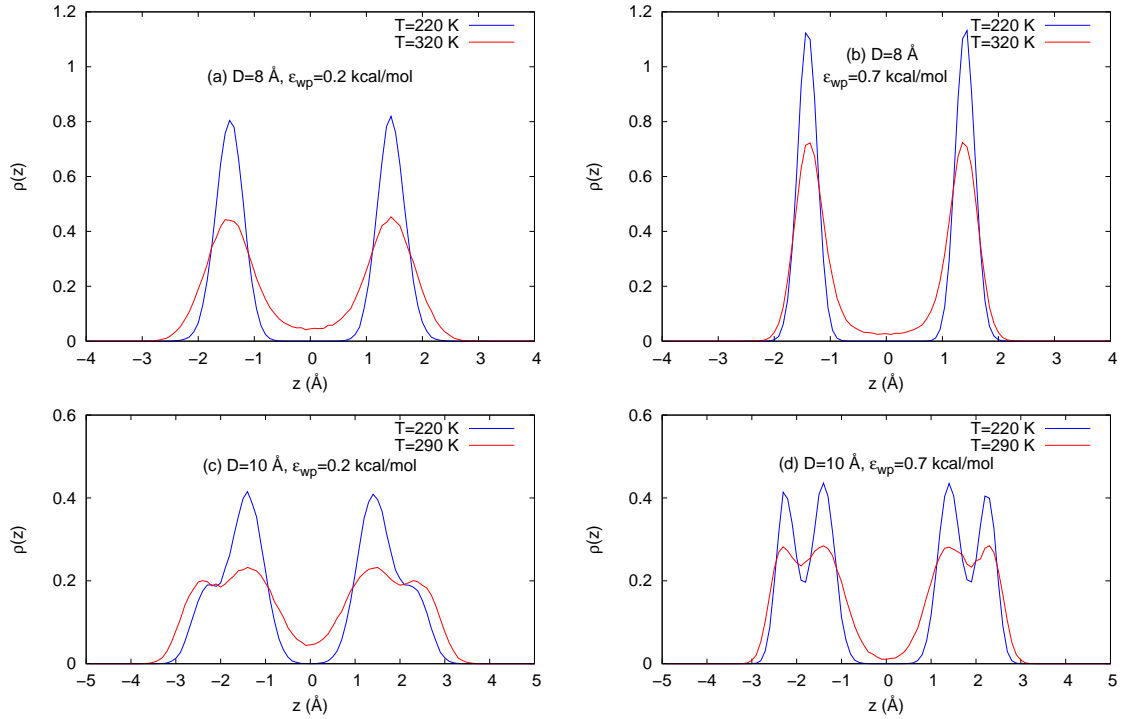
Figure 6.6: (a) and (b) The transverse density profiles, ρ_z, of systems with D=8 Å and ε_{wp}=0.2 and 0.7 kcal, respectively. (c) and (d) ρ_z of systems with D=10 Å and ε_{wp}=0.2 and 0.7 kcal, respectively.

single peak into two subpeaks indicates that at D=10 Å, the ice state becomes a puckered bilayer ice (referred to as the 2U structure [84]).

The profile of ρ_z of liquid states of systems with ε_{wp}=0.2 kcal/mol and 0.7 kcal/mol, with interplate distances D=8 and 10 Å, are shown in Fig. 6.6, along with the profiles of the correpsonding ice states. ρ_z of the liquid states have much wider distributions with smaller peaks at each layer center and with non-zero density across the slit center, indicating that water molecules in liquid states can move between two layers across the slit center, while the transverse movements of water molecules in the solid states are highly restricted.

Direct comparison of the ice configuration of the systems with D=8 and 10 Å and ε_{wp}=0.7 kcal/mol is shown in Fig. 6.7. The top views of ices at both D=8 and 10 Å exhibit similar hexagonal ice structure, with two layers in register. However, the side views clearly
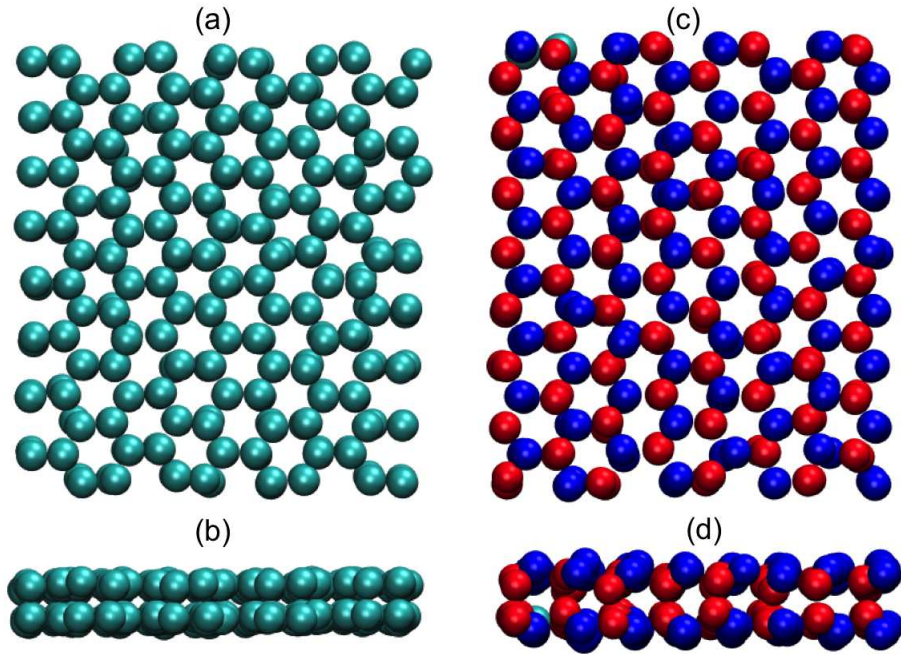
Figure 6.7: (a) Top view of a bilayer ice structure of a system with D=8 Å and ε_{wp} =0.7 kcal/mol at 220 K. (b) Side view of the same structure. The water molecules are colored in cyan. (c) and (d) The top and side view of bilayer ice structure of a system with D=10 Å and ε_{wp} =0.7 kcal/mol at 220 K. The water molecules on the outer sublayers are colored in dark blue and those on the inner sublayers are colored in red, and the rest are colored in cyan.

show the bilayer structure of the ice at D=8 Å is flat whereas the bilayer at D=10 Å exhibits a puckered structure. This explains why ρ_z displays two subpeaks within one main peak. The flat bilayer ice at D=8 Å allows each molecule to have four hydrogen-bonded neighbors. The top and side views of the bilayer ice structure at D= 8 Å demonstrate that the angle of neighbors within one layer is roughly $120°$ and the angle assumed by neighbors not all in one layer is roughly $90°$. The puckered bilayer structure at D=10 Å results in external sublayers with three hydrogen-bonded neighbors, while the molecules on the inner sublayers have four hydrogen-bonded neighbors. The angles formed by the neighboring molecules are roughly $109°$ for the ice structure at D=10 Å (something that is difficult to discern in the top and side views but apparent in the 3-dimensional ice structure).
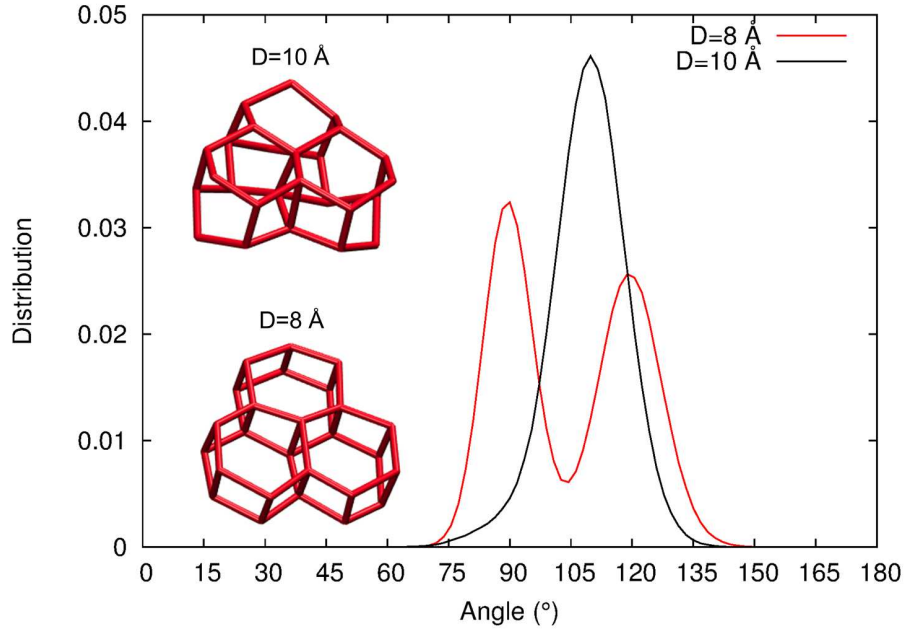
Figure 6.8: Distributions of angles formed by hydrogen-bonded neighbors in ice structures at D=8 Å (red) and 10 (black) with ε_{wp}=0.7 kcal/mol and T=220 K. Fragments of ice structure for D=8 and 10 Å are inserted, showing three adjacent rings in both layers.

Distributions of angles between hydrogen-bonded neighbors of ice structures at D=8 and 10 Å are shown in Fig. 6.8. Consistent with the impression made by inspection of the structures, the angle distribution of the ice structure at D=8 Å has two peaks located near 120° and 90°, corresponding to the angles formed within one layer and between two layers. These results agree with previous simulations [84] of ice structures at D=8 Å as well as experimental determination [103]. The angle distribution of the ice structure at D=10 Å, formed by angles for molecules with four or three hydrogen-bonded neighbors, has a single peak located near 109°, which is the signature value of tetrahedral geometry. As bulk ice Ih is characterized by hexagonal symmetry and near tetrehedral bonding angles, we recognize that the ice structure at D=10 Å is equivalent to a slice of ice Ih. Fig. 6.8 also displays fragments of the ice structures at D=8 and 10 Å, composed by three adject rings in both layers, which accentuate the flat hexagonal ring structure at D=8 Å and the

puckered hexagonal ring structure at D=10 Å.

6.4   Conclusion

Water nanofilms confined between plates, with the water-plate interaction parameter, $\varepsilon_{\mathrm{wp}}$=0.2, 0.3, 0.5, 0.7 kcal/mol, ranging from strongly hydrophobic to strongly hydrophilic, and five different interplate distances D=8, 8.5, 9, 9.5 and 10 Å, were simulated at lateral pressure equals to 1 atm, using a coarse-grained monatomic water model (mW). The solid-to-liquid phase transitions of the 20 systems were simulated with gREM to achieve enhanced sampling in the vicinity of the first-order phase transition through generalized ensemble sampling combined with the replica exchange paradigm.

The transition temperatures were derived for all 20 systems from the peaks in the isobaric heat capacity. For all values, $\varepsilon_{\mathrm{wp}}$, of the water-plate interaction strength, the transition temperature reaches a maximum at D=8.5 Å, and behaves parabolically around that interplate distance, in agreement with previous results [84]. At a given interplate distance D, the transition temperature is higher when $\varepsilon_{\mathrm{wp}}$ of the plate is higher, showing that for the water nanofilms confined between parallel plates, the transition temperature depends upon the affinity for the wall. Varying parameters for the interplate distance and water-plate interaction, D and $\varepsilon_{\mathrm{wp}}$, the transition temperature of the water nanofilm was observed to span a wide range of values from 240 K to 340 K.

The results of enthalpy-temperature curves show that both ice and liquid phases reach lower enthalpy states as the water-plate interaction strength, $\varepsilon_{\mathrm{wp}}$, increases from 0.2 to 0.7 kcal/mol. The phase change enthalpy, ΔH, volume, ΔV, and entropy, ΔS, of the water nanofilm with strong hydrophilic plate was observed to be higher than that of systems with strong hydrophobic plates, at all interplate distances from 8 to 10 Å. For both systems with hydrophobic and hydrophilic plates, as D increases from 8 to 9.5 Å, ΔH, ΔV, and ΔS decrease monotonically. However ΔS and ΔV show an increase again when D=10 Å for strong hydrophilic plates, indicating certain structural changes within the water nanofilm

as D increases to 10 Å.

We computed the transverse density profile, ρ_z, of the ice states of the 20 systems and observed two symmetric peaks in ρ_z for all systems. For D=8, 8.5, 9, 9.5 Å, each of the two peaks have Gaussian-like shapes, indicating the ice structures are flat bilayer ice. Furthermore, at a given D within this range, density peaks become higher and narrower as $\varepsilon_{\mathrm{wp}}$ increases from 0.2 to 0.7 kcal/mol, leading to more ordered ice structures. For D=10 Å, each of the main peaks of ρ_z split into two subpeaks, indicating the ice structure is a puckered bilayer ice. The heights of the external subpeaks grows as $\varepsilon_{\mathrm{wp}}$ increases, and become equivalent to the heights of the internal subpeaks when $\varepsilon_{\mathrm{wp}}$=0.7 kcal/mol.

We further characterized the ice structures of systems with D=8 and 10 Å and strong hydrophilic plates. The ice structure at D=8 Å is composed of flat hexagonal rings with nontetrahedral angles, the distribution of which has two peaks around 120° and 90°. The bilayer ice structure at D=10 Å is composed of hexagonal rings with near tetrahedral angles, the distribution of which has a single peak around 109°. This indicates that the ice structure at D=10 Å is a slab of bulk ice Ih, characterized by hexagonal symmetry and near tetrahedral bonding angles. The puckered bilayer ice, at $D = 10.5$ Å, was unstable with low melting temperature (210 K) at 1 atm lateral pressure, with the instability induced by the hydrophobic plate [84]. The solid-to-liquid transition temperature is as high as 275 K for the puckered bilayer ice at D=10 Å when $\varepsilon_{\mathrm{wp}}$=0.7 kcal/mol, showing that the puckered structure is stablized in a hydrophilic environment.

Chapter 7

Conclusion

7.1 Summary

We have extended gREM from the constant volume ensemble to the constant pressure ensemble to include volume fluctuation in molecular systems such as complex fluids and water. We applied gREM to simulations of phase transitions in a variety of systems undergoing strong phase transitions for which standard sampling techniques in the canonical ensemble are known to provide inadequate sampling. The detailed thermodynamic properties of diverse phase transitions were studied, including amorphous solid to liquid phase transition in the adapted Dzugutov system, liquid to vapor phase transition in Lennard fluids, and the solid to liquid phase transition in a water nanofilm. The thermodynamics of the phase transitions and structural properties of states in different phases, including the transition states, are investigated based on results from gREM simulations.

In the simulation of the phase transition from liquid to amorphous solid state in the adapted Dzugutov model systems, the measured rate of conformational sampling for gREM is similar to tREM. This results from the modest nature of the liquid to amorphous solid phase transition and the absence of a substantial enthalpy gap. The gradual nature of this phase change is in part due to fact that the amorphous solid state, lacks long-range translational order. As a result, the distribution of states in enthalpy is relatively continuous for temperature replicas as well as for the generalized enthalpy distributions.

The advantages of gREM are demonstrated in simulations of vapor-liquid phase transition in Lennard-Jones systems at low pressures, as the phase transition is associated with substantial changes in volume, enthalpy, and entropy. The canonical enthalpy distributions of tREM are disjoint, displaying an enthalpy gap corresponding to the large latent heat associated with the transition from vapor to liquid phase, and consequently the samplings of

the phase transition states are strongly impaired in tREM simulations. In contrast, gREM achieves comprehensive sampling in the phase transition region using generalized ensemble weights with a succession of unimodal enthalpy distributions, smoothly joining the vapor and liquid states. The unstable and metastable states in the canonical ensemble are transformed to stable states in gREM simulations, allowing direct inspection of states along the path of the phase transition, which provides additional insight into the underlying mechanism of the vapor-liquid phase transition.

The profile of the statistical temperature provided by gREM allows us for a clear distinction between first order and second order phase transitions, as the first order phase transition displays a signature S-loop in the statistical temperature. In the simulation of the liquid-solid phase transition in a bilayer water of varying density, a crossover from first-order (at low densities) to a continuous phase transition (at high densities) was observed in terms of a diminishing S-loop in the statistical temperature, consistent with other thermodynamic and structural indicators. The dependence of the thermodynamic properties related to phase transitions on the confinement environment of water nanofilms is investigated with gREM simulations. Remarkable sensitivity of the transition to the nature of the water-wall interaction is demonstrated, with implications for the understanding of interfacial and nano-confined water.

Extensive gREM simulations combined with ST-WHAM provide detailed thermodynamic properties intrinsic to phase transitions, including the transition temperature, heat capacity profile, phase change enthalpy, entropy, and volume. These thermodynamic properties can be accurately determined as enhanced sampling of the strong first-order phase transition region is achieved in gREM simulations.

7.2 Future Work

The power of gREM implemented with Monte Carlo (MC) simulations has been demonstrated through the applications to monatomic systems including the adapted Dzugutov

model, Lennard-Jones fluids, and coarsed-grained water. However, in condensed phase simulations of complex fluids and bimolecules, molecular dynamics (MD) is a more natural choice than Monte Carlo due to the difficulty in designing an effective algorithm for generating collective MC trial moves.

One future direction is to implement gREM in GROMACS, which is an open source MD simulation package widely used to simulate biomolecules. A major challenge to implement gREM into a MD simulation package is to have a correct scheme of temperature control of each replica and to handle the acceptence rules for replica exchanges and the force scaling depending on the scheme of temperature control. The thermostats should also be carefully chosen by investigating different combinations of temperature control and thermostats on the quality of enhanced sampling for strong phase transition.

The proper implementation of gREM in GROMACS can achieve enhanced sampling of the conformational space and thermodynamic properties of lipid bilayer, which would a significant contribution to the field. Lipid bilayers are known to assume multiple phases. As such, the simulation of phase change is essential to the complete characterization of the structural and thermodynamic properties of lipid bilayers as a function of thermodynamic parameters such as lipid composition and temperature. It will be fruitful to explore phases of lipid bilayers at physilogical temperature, and to study the phase transitions, those between solid (gel) and liquid phase, demonstrated by even single component lipid bilayers, as well as between liquid-ordered and liquid-disordered phases, associated with "lipid raft" formation on more complex lipid mixtures including cholesterol and sphingolipids.

Such studies will yield a detailed statistical model of the thermodynamics and kinetics of lipid bilayer phases, which has been a goal of many computational and experimental studies. The simulation of a pure lipid bilayer, for example, DPPC bilayers, will provide a benchmark of the performance of gREM implemented in GROMACS [22]. Following this, it will be meaningful to apply gREM to study the mixtures of lipids and cholesterol characteristic of most eukaryotic cell membranes. It will also be promising to employ gREM

in the simulation of self-assembly of aqueous Poly-Amido-Saccharide (PAS) amphiphiles, a novel polymer with the potential to serve as an effective biomaterials in applications including drug delivery.

Bibliography

[1] J. Vrabec, G. K. Kedia, G. Fuchs, and H. Hasse *Molecular Physics*, vol. 104, p. 1509, 2006.

[2] B. J. Berne and J. E. Straub *Current Opinion in Chemical Biology*, vol. 7, p. 181, 1997.

[3] A. Mitsutake, Y. Sugita, and Y. Okamoto *Biopolymers*, vol. 60, p. 96, 2001.

[4] H. Li, G. Li, B. A. Berg, and W. Yang *Journal of Chemical Physics*, vol. 125, p. 144902, 2006.

[5] B. A. Berg and T. Neuhaus *Physics Letters B*, vol. 267, p. 249, 1991.

[6] B. A. Berg and T. Neuhaus *Physical Review Letter*, vol. 68, p. 9, 1992.

[7] K. Hukushima and K. Nemoto *Journal of the Physical Society of Japan*, vol. 65, p. 1604, 1996.

[8] E. Marinari and G. Parisi *Europhysics Letters*, vol. 19, p. 451, 1992.

[9] C. J. Geyer and A. Thompson *Journal of the American Statistical Association*, vol. 90, p. 909, 1995.

[10] Y. Sugita and Y. Okamoto *Chemical Physics Letters*, vol. 314, p. 141, 1999.

[11] R. Zhou and B. J. Berne *Proceedings of the National Academy of Sciences of the United States of America*, vol. 99, p. 12777, 2002.

[12] H. Kamberaj and A. van der Vaart *Journal of Chemical Physics*, vol. 127, p. 234102, 2007.

[13] U. H. E. Hansmann *Chemical Physics Letters*, vol. 281, p. 140, 1997.

[14] P. A. Frantsuzov and V. A. Mandelshtam *Physical Review E*, vol. 72, p. 037102, 2005.

[15] P. Poulain, F. Calvo, R. Antoine, M. Broyer, and P. Dugourd *Physical Review E*, vol. 73, p. 056704, 2006.

[16] R. Yamamoto and W. Kob *Physical Review E*, vol. 61, p. 5473, 2000.

[17] E. Flenner and G. Szamel *Physical Review E*, vol. 73, p. 061505, 2006.

[18] B. A. Berg and T. Celik *Physical Review Letter*, vol. 69, p. 2292, 1992.

[19] A. E. Garcia and J. N. Onuchic *Proceedings of the National Academy of Sciences of the United States of America*, vol. 100, p. 13898, 2003.

[20] D. Paschek, S. Gnanakarnan, and A. E. Garcia *Proceedings of the National Academy of Sciences of the United States of America*, vol. 102, p. 6765, 2005.

[21] W. Zheng, M. Andrec, E. Gallicchio, and R. M. Levy *Proceedings of the National Academy of Sciences of the United States of America*, vol. 104, p. 15340, 2007.

[22] T. Nagai and Y. Okamoto *Molecular Simulation*, vol. 38, p. 437, 2012.

[23] D. J. Earl and M. W. Deem *Physical Chemistry Chemical Physics*, vol. 7, p. 3910, 2005.

[24] C. Zhang and J. Ma *Physical Review E*, vol. 76, p. 036708, 2007.

[25] E. Lyman, F. M. Ytreberg, and D. M. Zuckerman *Physical Review Letter*, vol. 96, p. 028105, 2006.

[26] M. R. Shirts and J. D. Chodera *Journal of Chemical Physics*, vol. 129, p. 124105, 2008.

[27] M. D'Agostino, F. Gulminelli, P. Chomaz, M. Bruno, F. Cannata, R. Bougault, F. Gramegna, I. Iori, N. L. Neindre, G. V. Margagliotti, A. Moroni, and G. Vannini *Physical Review B*, vol. 473, p. 219, 2000.

[28] M. Schmit, R. Kusche, T. Hippler, J. Donges, W. Kronmiller, B. von Issendorff, and H. Haberland *Physical Review Letter*, vol. 86, p. 1207, 2001.

[29] F. Calvo, D. J. Wales, J. P. K. Doye, R. S. Berry, P. Labastie, and M. Schmidt *Europhysics Letters*, vol. 82, p. 43003, 2008.

[30] J. P. K. Doye and D. J. Wales *Journal of chemical Physics*, vol. 102, p. 9673, 1995.

[31] D. J. Wales and J. P. K. Doye *Journal of chemical Physics*, vol. 103, p. 3061, 1995.

[32] R. M. Lynden-Bell and D. J. Wales *Journal of chemical Physics*, vol. 101, p. 1460, 1994.

[33] D. J. Wales and R. S. Berry *Physical Review Letter*, vol. 73, p. 2875, 1994.

[34] J. Kim, T. Keyes, and J. E. Straub *Journal of Chemical Physics*, vol. 132, p. 224107, 2010.

[35] A. M. Ferrenberg and R. H. Swendsen *Physical Review Letter*, vol. 63, p. 1195, 1989.

[36] J. Kim, T. Keyes, and J. E. Straub *Journal of Chemical Physics*, vol. 135, p. 061103, 2011.

[37] L. G. Rizzi and N. A. Alves *Journal of Chemical Physics*, vol. 135, p. 141101, 2011.

[38] M. Church, C. Ferry, and A. E. van Giessen *Journal of Chemical Physics*, vol. 136, p. 245102, 2012.

[39] M. Elenius and M. Dzugutov *Journal of Chemical Physics*, vol. 131, p. 104502, 2009.

[40] M. Elenius, T. Oppelstrup, and M. Dzugutov *Journal of Chemical Physics*, vol. 133, p. 174502, 2010.

[41] J. P. K. Doye, D. J. Wales, F. H. M. Zetterling, and M. Dzugutov *Journal of Chemical Physics*, vol. 118, p. 2792, 2003.

[42] J. A. Moriarty and M. Widom *Physical Review B*, vol. 56, p. 7905, 1997.

[43] N. W. Ashcroft and N. D. Mermin, *Solid State Physics.* Harcourt Brace and Co, 1976.

[44] D. Thirumalai and R. D. Mountain *Physical Review A*, vol. 42, p. 4574, 1990.

[45] E. B. Moore and V. Molinero *Journal of Chemical Physics*, vol. 130, p. 244505, 2009.

[46] J. J. Salacuse, A. R. Denton, and P. A. Egelstaff *Physical Review E*, vol. 53, p. 2382, 1996.

[47] J. N. Herrera, P. T. Cummings, and H. Ruiz-Estrada *Molecular Physics*, vol. 96, p. 835, 1999.

[48] P. J. Steinhardt, D. R. Nelson, and M. Ronchetti *Physical Review B*, vol. 28, p. 784, 1983.

[49] S. T. Y Wang and C. Dellago *Journal of Chemical Physics*, vol. 122, p. 214722, 2005.

[50] W. Lechner and C. Dellago *Journal of Chemical Physics*, vol. 129, p. 114707, 2008.

[51] F. Sciortino, P. Tartaglia, and E. Zaccarelli *Journal of Physical Chemistry B*, vol. 109, p. 21942, 2005.

[52] E. Bianchi, P. Tartaglia, E. L. Nave, and F. Sciortino *Journal of Physical Chemistry B*, vol. 111, p. 11765, 2007.

[53] Q. Lu, J. Kim, and J. Straub *Journal of Physical Chemistry B*, vol. 116, p. 8654, 2012.

[54] B. Smit *Journal of Chemical Physics*, vol. 96, p. 8639, 1992.

[55] V. G. Baidakov, S. P. Protsenko, Z. R. Kozlova, and G. G. Chernykh *Journal of Chemical Physics*, vol. 126, p. 214505, 2007.

[56] X. C. Zeng and D. W. Oxtoby *Journal of Chemical Physics*, vol. 94, p. 4472, 1991.

[57] J. R. Errington *Journal of Chemical Physics*, vol. 118, p. 9915, 2003.

[58] A. R. Imre, G. Mayer, G. Hazi, R. Rozas, and T. Kraska *Journal of Chemical Physics*, vol. 128, p. 114708, 2008.

[59] V. V. Brazhkin, Y. D. Fomin, A. G. Lyapin, V. N. Ryzhov, and E. N. Tsiok *Journal of Physical Chemistry B*, vol. 115, p. 14112, 2011.

[60] P. R. ten Wolde and D. Frenkel *Journal of Chemical Physics*, vol. 109, p. 9901, 1998.

[61] M. P. Allen and D. J. Tildesley, *Computer Simulation of Liquids.* Clarendon, 1987.

[62] D. Frenkel and B. Smit, *Understanding Molecular Simulation: From Algorithms to Applications.* Academic, 1996.

[63] J. Frenkel, *Kinetic Theory of Liquids.* Dover, 1955.

[64] F. F. Abraham, *Homogeneous Nucleation Theory.* Academic, 1974.

[65] K. Binder and D. Stauffer *Advances in Physics*, vol. 25, p. 343, 1976.

[66] P. R. ten Wolde, M. J. Ruiz-Montero, and D. Frenkel *Journal of Chemical Physics*, vol. 110, p. 1591, 1999.

[67] M. Schrader, P. Virnau, and K. Binder *Physical Review E*, vol. 79, p. 061104, 2009.

[68] T. B. Woolf, D. M. Zuckerman, N. Lu, and H. Jang *Journal of Molecular Graphics and Modelling*, vol. 22, p. 359, 2004.

[69] P. Bhimalapuram, S. Chakrabarty, and B. Bagchi *Physical Review Letters*, vol. 98, p. 206104, 2007.

[70] J. Wedekind, G. Chkonia, J. Wolk, R. Strey, and D. Reguera *Journal of Chemical Physics*, vol. 131, p. 114506, 2009.

[71] J. E. Lennard-Jones *Proceedings of the Royal Society of London. Series A*, vol. 106, p. 441, 1924.

[72] S. Trebst, M. Troyer, and U. H. E. Hansmann *Journal of Chemical Physics*, vol. 124, p. 174903, 2006.

[73] E. A. Guggenheim *Journal of Chemical Physics*, vol. 91, p. 461, 1945.

[74] D. Chandler, *Introduction to Modern Statistical Mechanics*. Oxford, 1987.

[75] H. S. Ashbaugh *Journal of Chemical Physics*, vol. 130, p. 204517, 2009.

[76] H. B. Callen, *Thermodynamics: An Introduction to the Physical Theories of Equilibrium Thermostatics and Irreversible Thermodynamics*. John Wiley and Sons, 1985.

[77] F. H. Stillinger *Journal of Chemical Physics*, vol. 38, p. 1486, 1963.

[78] L. G. MacDowell, V. K. Shen, and J. R. Errington *Journal of Chemical Physics*, vol. 125, p. 034705, 2006.

[79] R. Godawat, S. N. Jamadagni, J. R. Errington, and S. Garde *Industrial and Engineering Chemistry Research*, vol. 47, p. 3582, 2008.

[80] E. B. Moore and V. Molinero *Journal of Chemical Physics*, vol. 130, p. 244505, 2009.

[81] L. Le and V. Molinero *Journal of Physical Chemistry A*, vol. 115, p. 5900, 2011.

[82] E. B. Moore and V. Molinero *Nature (London)*, vol. 479, p. 506, 2011.

[83] A. Reinhard and J. P. K. Doye *Journal of Chemical Physics*, vol. 136, p. 054501, 2012.

[84] N. Kastelowitz, J. C. Johnston, and V. Molinero *Journal of Chemical Physics*, vol. 132, p. 124511, 2010.

[85] E. B. Moore, J. T. Allen, and V. Molinero *Journal of Physical Chemistry C*, vol. 116, p. 7507, 2012.

[86] J. C. Johnston, N. Kastelowitz, and V. Molinero *Journal of Chemical Physics*, vol. 133, p. 154516, 2010.

[87] R. C. DeMille, T. E. Cheatham, and V. Molinero *Journal of Physical Chemistry B*, vol. 115, no. 1, p. 132, 2011.

[88] A. H. Nguyen and V. Molinero *Journal of Physical Chemistry B*, vol. 117, p. 6330, 2013.

[89] S. Han, M. Y. Choi, P. Kumar, and H. E. Stanley *Nature Physics*, vol. 6, p. 685, 2010.

[90] J. Bai and X. C. Zeng *Proceedings of the National Academy of Sciences of the United States of America*, vol. 109, p. 21240, 2012.

[91] A. A. Bakulin, D. Cringus, P. A. Pieniazek, J. L. Skinner, T. L. C. Jansen, and M. S. Pshenichnikov *Journal of Physical Chemistry B*, vol. 117, no. 49, p. 15545, 2013.

[92] N. Giovambattista, P. J. Rossky, and P. G. Dbenedetti *Physical Review Letter*, vol. 5, p. 050603, 2009.

[93] K. Koga, G. T. Gao, H. Tanaka, and X. C. Zeng *Nature*, vol. 412, p. 802, 2001.

[94] P. Kumar, S. V. Buldyrev, F. W. Starr, N. Giovambattista, and H. E. Stanley *Physical Review E*, vol. 72, p. 051503, 2005.

[95] Z. Li and H. A. Scheraga *Proceedings of the National Academy of Sciences of the United States of America*, vol. 84, p. 6611, 1987.

[96] D. J. Wales and J. P. K. Doye *The Journal of Physical Chemistry A*, vol. 101, p. 5111, 1997.

[97] J. Nocedal *Mathematics of Computation*, vol. 35, p. 773, 1980.

[98] D. Liu and J. Nocedal *Mathematical Programming*, vol. 45, p. 503, 1989.

[99] Z. Li and H. A. Scheraga *Proceedings of the National Academy of Sciences of the United States of America*, vol. 84, no. 19, p. 6611, 1987.

[100] D. J. Wales and J. P. K. Doye *Journal of Physical Chemistry A*, vol. 101, no. 28, p. 5111, 1997.

[101] D. J. Wales and H. A. Scheraga *Science*, vol. 285, no. 5432, p. 1368, 1999.

[102] F. H. Stillinger and T. A. Weber *Physical Review B*, vol. 31, p. 5262, 1985.

[103] G. A. Kimmel, J. Matthiesen, M. Baer, C. J. Mundy, N. G. Petrik, R. S. Smith, Z. Dohnálek, and B. D. Kay *Journal of the American Chemical Society*, vol. 131, no. 35, p. 12838, 2009.

Curriculum Vitae